Title
Interfacial Engineering of Molecular Photovoltaics

Author
Shelton, Steven Wade

Publication Date
2014

Peer reviewed|Thesis/dissertation

Interfacial Engineering of Molecular Photovoltaics

by

Steven Wade Shelton

A dissertation submitted in partial satisfaction of the

requirements for the degree of

Doctor of Philosophy

in

Engineering – Materials Science and Engineering

in the

Graduate Division

of the

University of California, Berkeley

Committee in charge:
Professor Junqiao Wu, Co-chair
Professor Biwu Ma, Co-chair
Professor Oscar Dubon
Professor Ana Arias

Spring 2014

Interfacial Engineering of Molecular Photovoltaics

Abstract

Interfacial Engineering of Molecular Photovoltaics
by
Steven Wade Shelton
Doctor of Philosophy in Engineering – Materials Science and Engineering

University of California, Berkeley
Professor Junqiao Wu, Co-chair
Professor Biwu Ma, Co-chair

One of the most worthy pursuits in the field of organic solar cells is that of discovering ways to more effectively harvest charge generated by light absorption. The measure of the efficacy of this process is the external quantum efficiency (EQE). It is determined by the efficiency of incident light absorption, exciton diffusion, exciton splitting and charge transfer, and charge collection. Enhanced EQE can be realized by engineering interfaces between materials in the device to allow for smoother charge transfer throughout the extent of the device, which is usually between 10 and 200 nanometers. Improvements in charge transport are vitally important because the photogenerated excitons in electron donating polymers and small molecules typically only diffuse between 5 and 10 nanometers. These excitons must reach the interface between the electron donor and electron acceptor in order to be split so that the resulting electron and hole can be harvested at the cathode and anode, respectively.

The aim of much of this dissertation is to describe a method by which the donor-acceptor interfacial area can be augmented using nanoimprint lithography, first with a single donor and then with multiple donors. Nanoimprint lithography is introduced as a simple embossing technique that can create features in a single component donor with dimensions as small as 20 nm. Solution-processable small molecules are of interest for their ease of synthesis and fabrication. I continue the discussion of nanoimprint lithography by offering candidates for a two-component donor combination. A two-component donor can extend the absorption range across a broader portion of the solar spectrum than just one donor to improve energy harvesting.

After considering ways of optimizing the donor-acceptor interface, I describe the use of a charge selective layer for better charge transport and collection. When incorporated into a bilayer solar cell and an inverted solar cell, these two molecules markedly improve the energy conversion efficiency.

Contents

Acknowledgements

During the five and a half years of graduate work culminating in this dissertation, there have been many people to provide inspiration, knowledge, wisdom, and support to encourage my effort. I'd like to acknowledge many of them and thank them for their consideration.

I thank my research advisor, Prof. Biwu Ma, for the chance to study under his tutelage and learn the mechanics of research. I appreciate how open and understanding he has been while I learn the complicated scientific enterprise. I also appreciate the assistance of my academic advisor, Prof. Junqiao Wu, who offered advice at the most critical junctures of my tenure at UC Berkeley.

My day to day work was facilitated by the very capable students and staff at the Molecular Foundry at Lawrence Berkeley Lab. Sibel Leblebici and Teresa Chen have been both friends and able colleagues who were invaluable to my progress over the past several years. The same can be said about Xiaodan Gu. I cannot imagine my tenure at Berkeley without their intellect, input, and, most importantly, sense of humor. Deirdre Olynick was also instrumental in my work with Xiaodan and her advice expedited many of the results seen in this dissertation.

Of course, there are many people who have provided a wealth of information to help me make more informed decisions. Most notably, I'd like to thank Chris Hahn, Sean Andrews, Michael Moore, Melissa Fardy, Ziyang Huo, Erik Garnett, and Akram Boukai, who all took it upon themselves as experienced researchers to show me the ropes in some capacity.

The professors who have most directly contributed to my tenure here are Prof. Oscar Dubon, Prof. Ana Arias, Prof. Ali Javey, Prof. Andy Minor, and Prof. Andreas Glaeser. I thank Profs. Dubon, Arias, Javey, and Minor for helpful discussions regarding my qualifying exam. I also thank Prof. Glaeser because he left a lasting impression on me at Admit Weekend by letting me know that he would make my stay here as comfortable as possible. I especially thank Prof. Alex Briseno of the University of Massachusetts, Amherst for an immense amount of knowledge, wisdom and faith that I could be greater than I am no matter the setbacks, of which there have been many. Alex helped me arrive to the most important point a scientist can reach; that is the point at which he can make an original contribution.

Lastly, I'd like to thank my family, both immediate and otherwise, who always have kind and supportive words for me during my educational pursuits. I have a mother, Bonita, who loves me whether I succeed or fail. I appreciate that fact more and more every year as I seem to be getting better at the latter. I also have a sister, Nikki, who has lent a helping hand as I overcame personal obstacles as a graduate student. I am very fortunate to have such a supportive family.

Chapter 1

Introduction to Organic Photovoltaics

1.1 A Brief History

Thin film solar cells have been intensely studied since the 1980s for scientific and commercial pursuits. After the energy crisis of the 1970's there was a shift in the scope of solar energy research from expensive crystalline silicon-based photovoltaic (PV) modules to modules that could use alternative, cheaper materials. Some of the popular candidate materials included, Cu_2S, CdS, and CdTe. C. W. Tang of Kodak initiated another shift when he demonstrated the photovoltaic effect in organic small molecules at Kodak in 1986, converting power at 1% efficiency.[1] The basic operational principles of organic solar cells is shown in Fig. 1. Upon light absorption, a bound electron-hole pair, or exciton, is generated in the donor. This exciton diffuses to the interface between the donor and acceptor before being split. At this time, the electron is transferred to the acceptor. The electron continues to drift through the acceptor to the cathode while the hole drifts through the donor to the anode. Organic materials have important

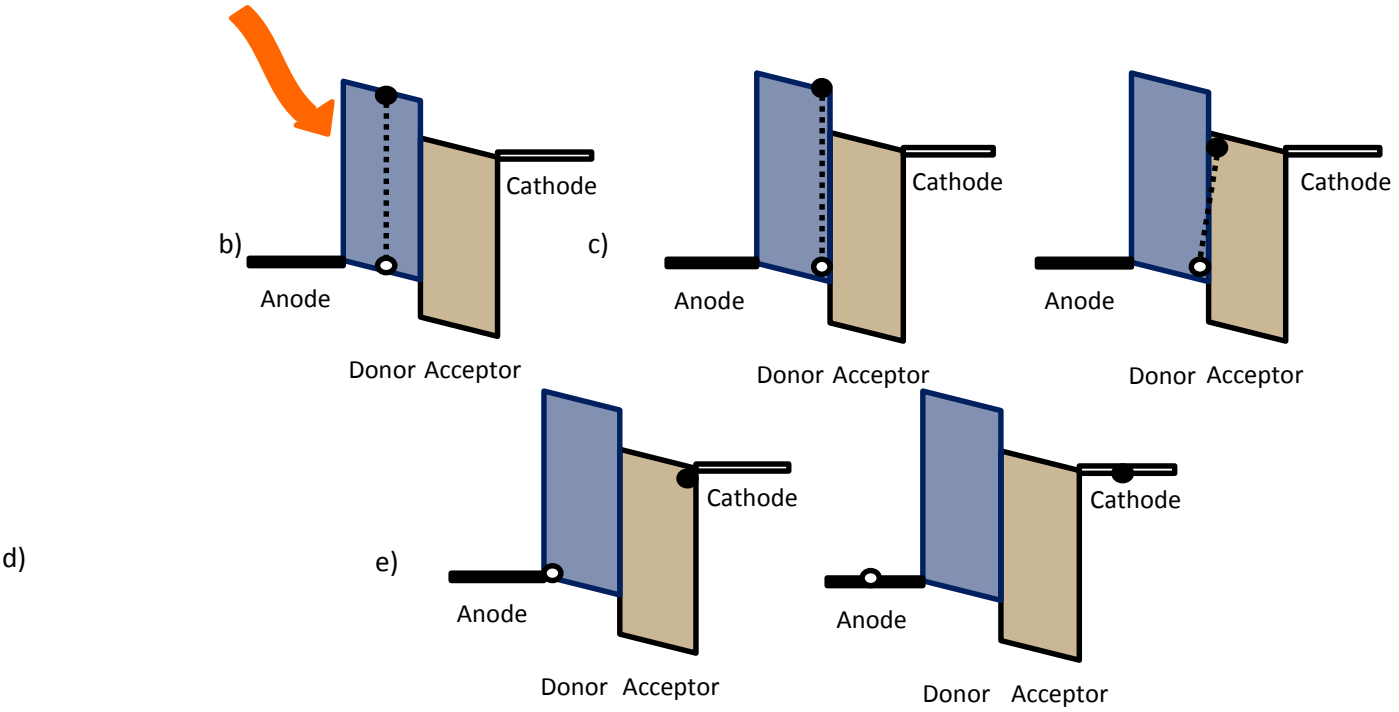

Fig. 1 Band diagram of an organic solar cell constructed with a donor (blue) and acceptor (tan) sandwiched between an anode and cathode: a) exciton formation (electron is black and hole is white) under illumination; b) exciton diffusion to the donor-acceptor interface; c) electron transfer to the acceptor; d) charge drift to the electrodes; and e) charge collection at the electrodes.

characteristics distinct from inorganic materials. Organic materials tend to have higher absorption coefficients and chemical tunability. Moreover, organic PV modules can be flexible and, thus, conform to a variety of surfaces. During the 1980's and 1990's polymer-based solar cells were extensively studied in addition to molecular solar cells to determine the operating principles of organic solar cells. Contrary to a silicon-based module which achieves charge separation at the junction of p-type silicon and n-type silicon, an organic solar cell achieves charge separation at the junction of an electron donor and electron acceptor. Furthermore, this charge separation at the donor-acceptor heterojunction is more effective if the donor and acceptor are intimately mixed, as discovered by Yu *et. al.* in 1995, resulting in a power conversion efficiency of 3%.[2] Yu blended poly(2-methoxy-5(2'-ethyl-hexyloxy)-(1,4-phenylene vinylene) (MEH-PPV) and [6,6]-phenyl-C61-butyric acid methyl ester (PCBM) to create a bulk heterojunction with substantially more donor-acceptor interface.

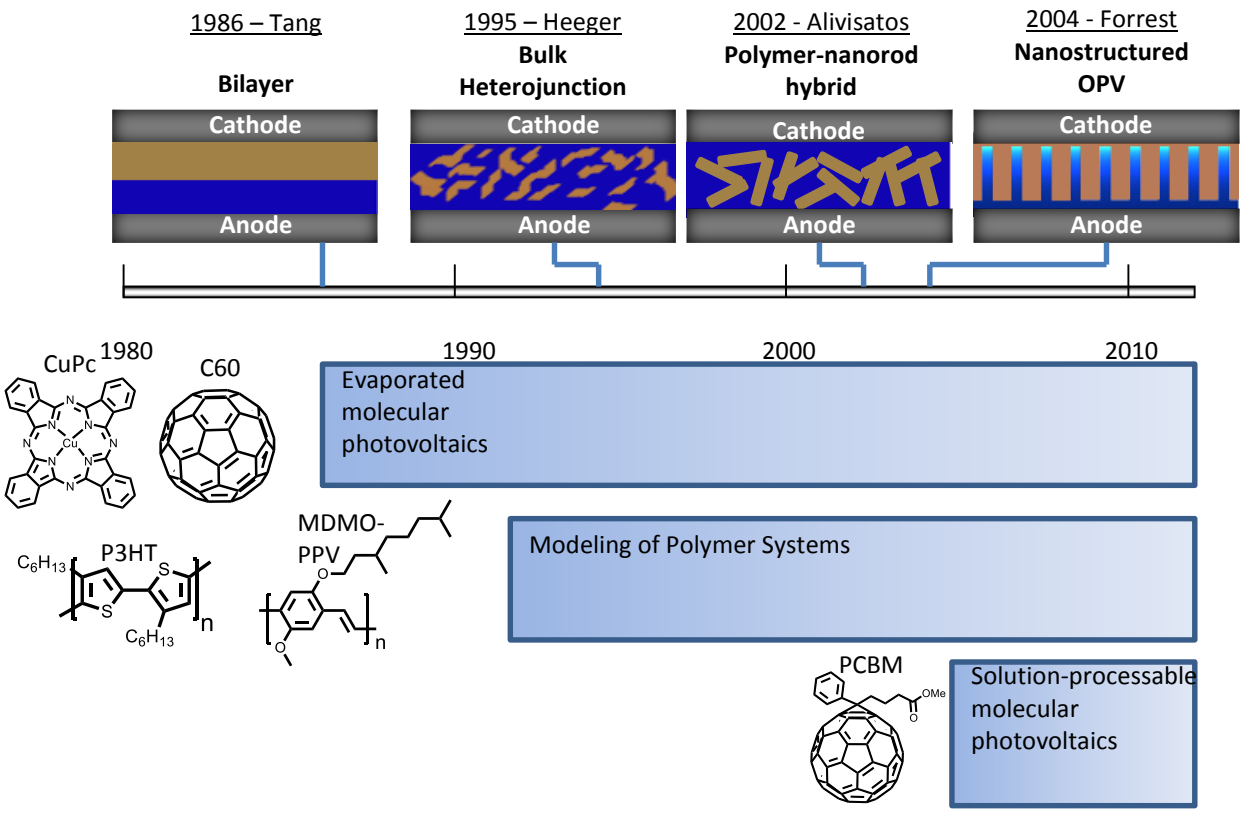

Fig. 2 Timeline showing important advances in the architecture and materials systems employed by organic photovoltaic cells.

This and other important advances during the 1990's (Fig. 2) were made as the fundamental device physics of organic solar cells were still being uncovered. In addition to MEH-PPV and PCBM, another workhorse polymeric material was poly(3-hexylthiophene) (P3HT) and a commonly used small molecule was copper phthalocyanine (CuPc). Among the

important distinctive properties of organic photoactive materials is that light generates a coulombically bound electron-hole pair rather than a free electron-hole pair as in inorganic materials. The dielectric constant tends to be much lower in organic materials like P3HT (ε = 3-4) than inorganic materials like silicon (ε = 11) so the electron and hole are ineffectively screened from one another and, thus, bound with energy typically of .4-1.4 eV.[3,4] Moreover, this bound electron-hole pair only diffuses a paltry 3-10 nm in most organic semiconductors. If it does not reach a donor-acceptor interface, it will recombine and reemit radiation. If it does, however, reach an interface, and there is sufficient energetic difference, about .3 eV at least, then it will be energetically favorable for the electron to transition from the donor to the acceptor and the exciton can be split. The electron will then drift to the cathode and the hole will drift to the anode. Importantly, the dissociated carriers must be whisked away at a sufficient rate to prevent charge back transfer and electron-hole recombination. The mobility gives a sense of how quickly charge can move through the disordered organic network. Because the mobility is quite low relative to that of inorganic materials, typically 10^{-4}-10^{-3} $cm^2/V\bullet s$, electric charges can accumulate in certain portions of the active layer as they traverse the film. This behavior leads to a build-up of space charge which can impede further flow of current. The space-charge limited current is expressed in the following way:[5]

$$J = \frac{9}{8}\varepsilon_r\varepsilon_0\mu_h\frac{V^2}{L^3} \tag{1.1}$$

where ε_r is the relative permittivity, ε_0 is the vacuum permittivity, μ_h is the hole mobility, V is the voltage, and L is the thickness of the donor. While this equation holds when the mobility, itself, is field-independent, there is an alternate expression when the mobility is field-dependent:[5]

$$J = \frac{9}{8}\varepsilon_r\varepsilon_0\mu_{h0}e^{.89\gamma\sqrt{E}}\frac{V^2}{L^3} \tag{1.2}$$

where μ_{h0} is the zero-field mobility. Once the charges have drifted according to one of these relationships, it can be collected at the electrode. Thus, the efficiency with which absorbed light generates charge, the internal quantum efficiency, is described by the efficiency of light absorption (η_A), exciton diffusion (η_{ED}), exciton splitting and charge transfer (η_{CT}), and charge collection (η_{CC}); stated algebraically:

$$\eta_{IQE} = \eta_A\eta_{ED}\eta_{CT}\eta_{CC.} \tag{1.3}$$

One can account for the efficacy with which incident light is coupled to the device, which might be diminished by scattering, by calculating the external quantum efficiency (EQE), or the ratio of electrons collected to incident photons. EQE is given by

$$\eta_{EQE} = (1-R)\eta_A\eta_{ED}\eta_{CT}\eta_{CC}. \tag{1.4}$$

The most important figures of merit of solar cell performance are gleaned from a current-voltage sweep of the device in the dark and in the light (Fig. 3). The figures of merit immediately observable on the plot of the current density under illumination are the short circuit current (J_{sc}) and open circuit voltage (V_{oc}). The former is seen where the applied voltage is zero while the latter is seen where the current density is zero. The black dashed lines in Fig. 3 intersect at the maximum power point, where the product of voltage and current density is highest. The ratio of the maximum power to the product of J_{sc} and V_{oc} yields the fill factor (FF) according to the following relation:

$$\frac{(IV)_{max}}{I_{sc}V_{oc}} = FF. \tag{1.5}$$

Finally, the overall energy conversion efficiency (η) is calculated according to the relation,

$$\frac{(IV)_{max}}{P_{sun}} = \eta \tag{1.6}$$

where P_{sun} is the incident solar power.

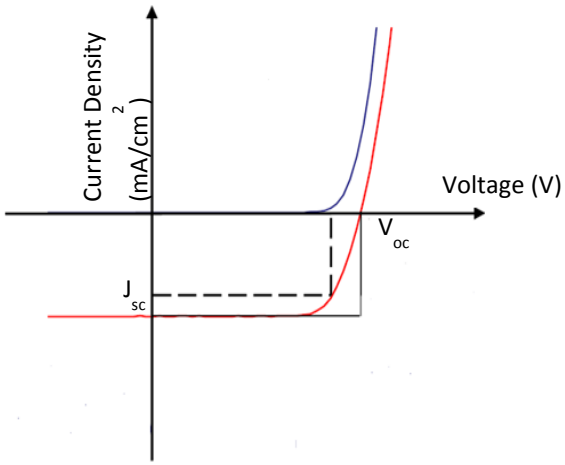

Fig. 3 Current-voltage sweep of an organic solar cell in the dark (blue) and in the light (red).

Improvements to organic solar cells tend to pertain to a few general areas, including materials development, morphology, and interface modification. Clearly, extending the absorption range using low-bandgap constituents like the polymer poly[2,6-(4,4-bis-(2-ethylhexyl)-4*H*-cyclopenta[2,1-*b*;3,4-*b*']dithiophene)-alt-4,7-(2,1,3-benzothiadiazole)](PCPDTBT)[6] and the small molecule B,O-chelated azadipyrromethene (BO-ADPM) can allow the solar cell to more completely utilize the solar spectrum.[7] In contrast to these efforts, some developments are aimed at increasing the mobility of organic semiconductors, as exhibited by the synthesis by Yang of poly(4,4-dioctyldithieno(3,2-b:2',3'-d)silole)-2,6-diyl-alt-(2,1,3-benzothiadiazole)-4,7-diyl) (PSBTBT).[8] The efforts regarding morphology have focused on creating the best packed structure of donor and acceptor,[9] conventionally with annealing techniques.[10]

1.2 Objectives

The efforts described in this dissertation deal specifically with interface engineering, particularly at the junction between the active layers and the electrode and within the active layer itself. The engineering within the active layer seeks to address key deficiencies of organic semiconductors: poor exciton diffusion and narrow absorption. Since excitons are able to diffuse in a very limited volume, it is critical to have a donor-acceptor interface in the vicinity of every exciton to improve exciton quenching and charge collection. It is commonly accepted that an ordered, nanostructured morphology between the donor and acceptor is ideal for this purpose (Fig. 4). Herein, a method for achieving such nanostructured morphology, nanoimprint lithography, will be detailed. Next, a method for nanostructuring a two-component donor will be discussed to show how the absorption spectrum of the device can be broadened with a donor that absorbs in different wavelength ranges. Finally, efforts to improve charge collection at the junction of the donor and the anode using a molecular hole-injection layer will conclude the experimental results of the dissertation.

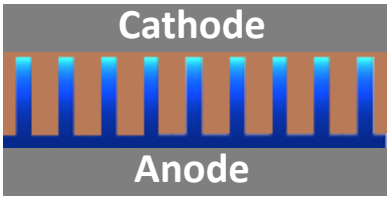

Fig. 4 Diagram of an organic solar cell with nanostructured donor (blue) and acceptor (tan).

Small molecules are the focus of this dissertation for several reasons. The advantages of small molecules compared to polymers include their monodispersity, ease of synthesis and high purity. Small molecules also tend to pack better than polymers since they tend to have fewer

bulky side chains that disturb such packing. For this reason, small molecules tend to crystallize into larger grains, raising the mobility. Though the first organic heterojunction solar cell incorporated small molecules, molecular solar cells did not receive the most attention during the 1990's. The popular donor materials were polymers like P3HT and MEH-PPV and these materials formed the basis of a much of the experimental work to understand the device physics of organic solar cells. Nonetheless, molecular acceptors such as C60 and PCBM were a staple of these solar cells because they accept electrons so readily and allow excitons to be split on extremely short time scales (femtosecond). This is in no small part due to the success of the bulk heterojunction based on polymers and PCBM, which are both easily processed in solution. It was not until Yang demonstrated an efficient molecular bulk heterojunction in 2005 that interest resurged in molecular photovoltaics.[11] There was another surge after Lloyd *et. al.* set forth a library of interesting solution-processable small molecules, which paved the way for easier fabrication of molecular photovoltaics.[12] A fully solution-processable active layer would allow for roll-to-roll processing and flexible solar panels, which is a particularly attractive option for certain applications like military usage. The results put forth in this dissertation set forth methods to enhance exciton splitting by donor-acceptor interface engineering, augment absorption by tailoring the interface between two suitable donors, and more readily accept charges by altering the donor-anode interface.

Chapter 2

Nanoimprinting of a Small Molecule Donor Layer

2.1 Nanostructuring Strategies

Several novel techniques for generating organic nanostructures have been demonstrated recently. Hirade *et. al.* employed a seeded growth method in which a thin layer of 3,4,9,10-perylene-tetracarboxlyic-dianhydride (PTCDA) (3nm)/CuPc (3nm) was deposited before CuPc was further deposited by sublimation (Fig. 5).[13] It is important to first deposit the PTCDA layer because it orients face-on to the substrate; CuPc naturally prefers to orient edge-on. Once the correct orientation is established by the seed, CuPc can continue to growth vertically from the substrate.

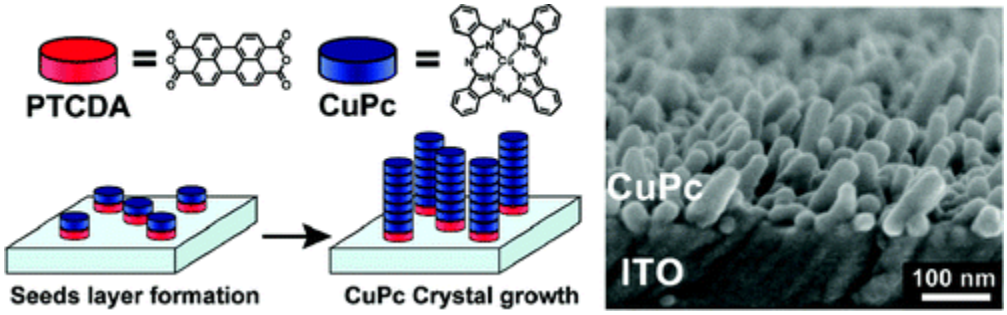

Fig. 5 – Nanopillars of CuPc on PTCDA grown by vacuum.[13]

Alternatively, one can use the self-organizing properties of block copolymers (BCP) to arrange the donor and acceptor in a favorable orientation. Taking advantage of the fact that block-copolymers can arrange themselves in a variety of orientations depending on the relative molecular weight of each block, photovoltaic developers have identified two particularly useful morphologies for solar cells: layered and cylindrical (Fig. 6). Both methods of phase segregation allow for a continuous percolation pathway for the hole and electron in the donor and acceptor material, respectively. In these arrangements, it is critical to insert a hole-selective layer between the donor material and the anode and an electron-selective layer between the acceptor and cathode.

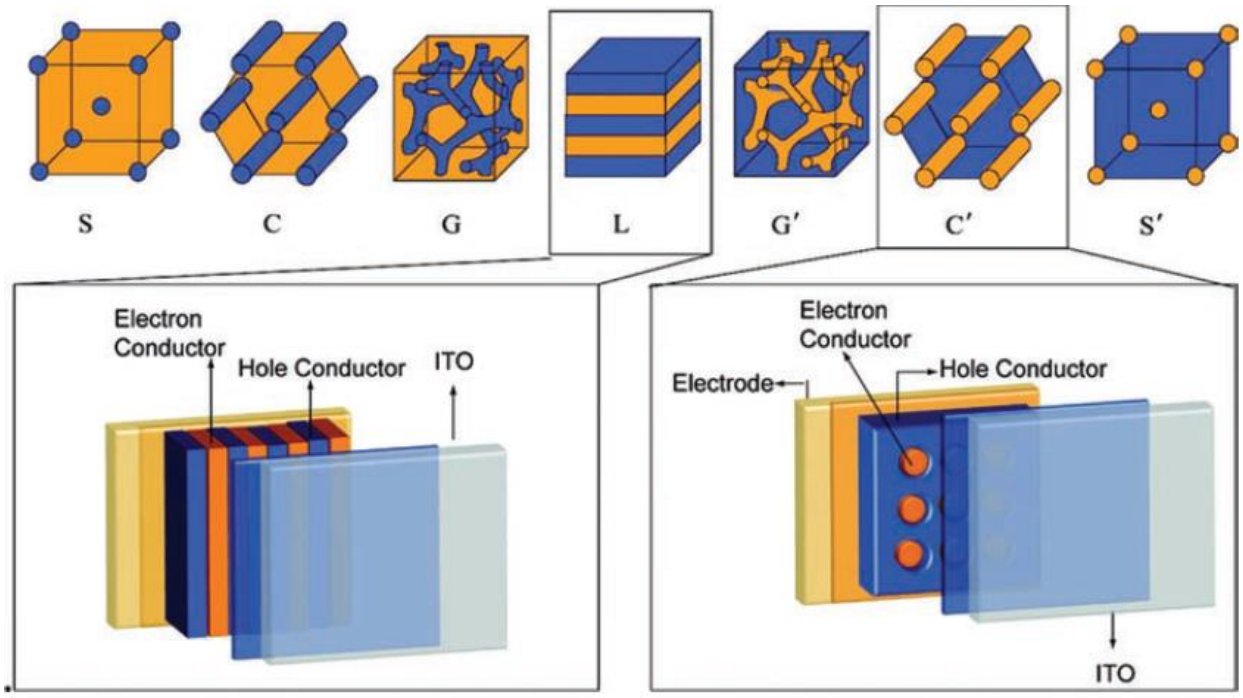

Fig. 6 (Top) various morphologies of a block-copolymer dependent on the relative molecular weights of each block.[14]

Yet another way to generate organic nanostructures is with a top-down approach using a templated mask. A di-block copolymer with cylindrical morphology can be used to generate a hard template if it is spin-cast onto silicon. Polystyrene-block-poly(ethylene oxide) (PS-*b*-PEO, 32k-*b*-11k), for example, orients into cylinders of PEO roughly 20nm in diameter surrounded by a matrix of PS. Of course, the domain size, D, can be tailored by altering the number of monomers in each block, N, according to the relation

$$D \propto aN^{2/3}\chi^{1/6} \tag{1.7}$$

for which a is the segment length and χ is the Flory-Huggins interaction parameter.[15] This film can be reconstructed by soaking in ethanol such that the PEO is mostly displaced to the surface. After a brief exposure to oxygen plasma, PEO is removed, leaving cylindrical holes in a PS matrix. Further etching via inductively coupled plasma (ICP) of SF_6/O_2 etches pores into the underlying silicon substrate (Fig. 7).

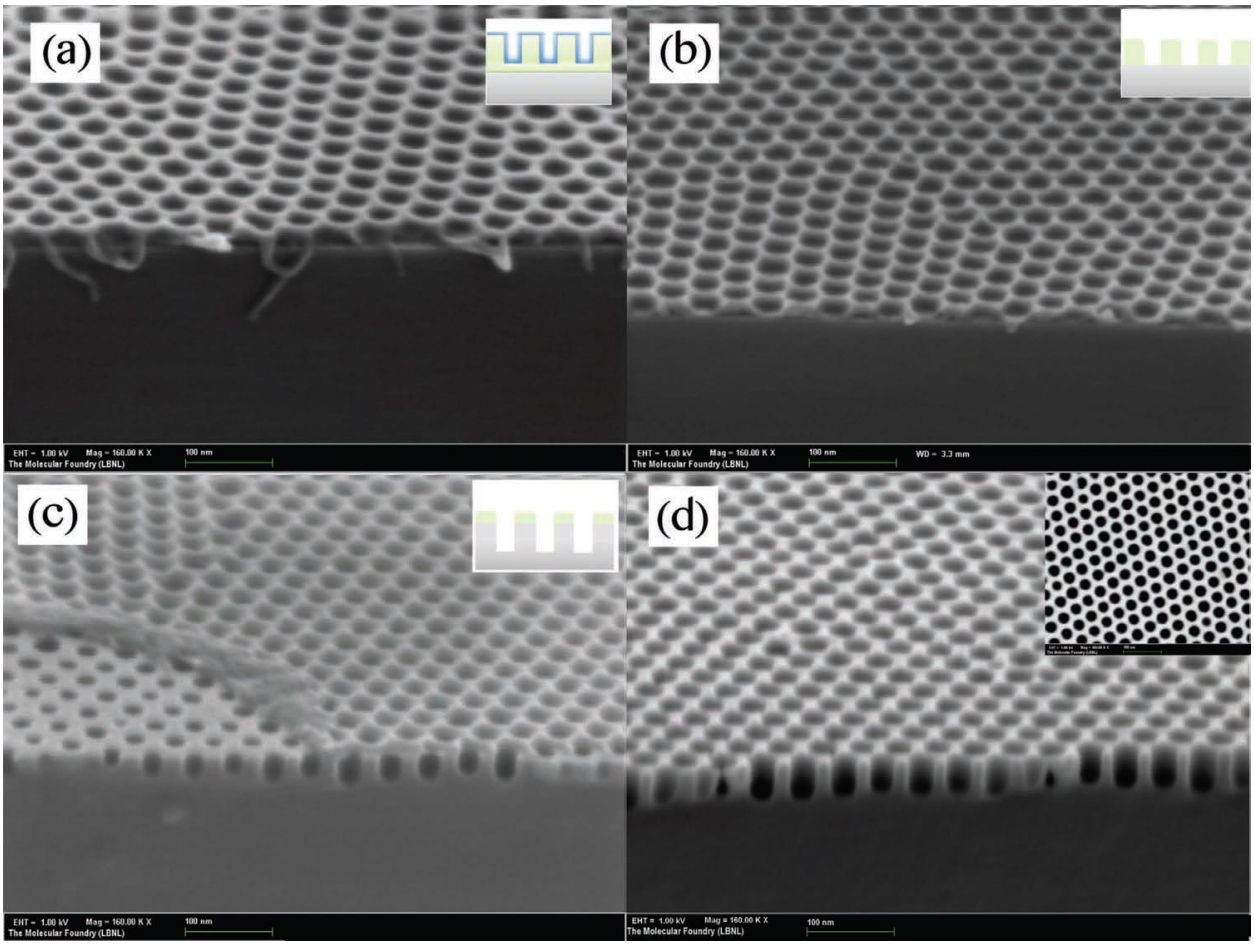

Fig. 7 a) Block copolymer pattern after solvent annealing and ethanol reconstruction. b) BCP film after being etched for 10 s in RIE c) Pattern etched into silicon with 10 s of cryo-ICP etching d) Silicon pattern after a full 20 s of cryo-ICP etching[16]

Once the silicon template is created, it can be used to pattern soft materials. The method for doing so is nanoimprint lithography. Commercially available polymers have long been used as both the patterned material, such as a resist, and as a soft replica of a hard mold. Of course, the process of nanoimprint lithography is not only compatible with polymers, but with small molecules as well. The first step of nanoimprint lithography is to identify the temperature at which the material is soft enough to conform to a mold; the glass transition temperature, T_g, is typically chosen. Differential scanning calorimetry can measure this quantity. It is also important to know the decomposition temperature, as determined by thermogravimetric analysis. With both temperatures, one can chose a processing temperature greater than the glass transition temperature but less than the decomposition temperature. Next, a pristine film of the organic material is spin-cast onto the substrate. The etched silicon template, pre-coated with an anti-sticking layer, is pressed against the material while it is heated in a way such that the mask maintains a constant pressure. As the material softens under the influence of heat, the template

deforms the material to generate nanopillars within the hollow cylinders. The sample is then cooled and the mask peeled away. Due to the anti-sticking layer, the mask can be removed while preserving the integrity of the film.

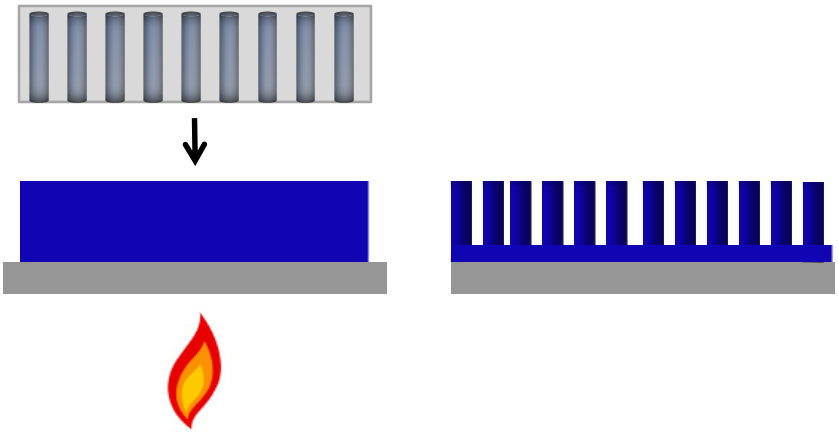

Fig. 8 Schematic showing how a silicon mask (gray) with cylindrical features transfers its pattern to the soft organic material (blue).

2.2 Experimental Plan for Nanoimprint Lithography

There are guidelines for how to tailor the dimensions. First, the nanopillars should be long enough to absorb 90% of the incident light. With the aid of the Beer-Lambert Law,

$$\frac{I}{I_0} = e^{-\propto l} \tag{1.8}$$

one can calculate the optimal pillar length. In the above relationship, I_0 is the incident light intensity, I is the transmitted intensity of light, α is the absorption coefficient at a specific wavelength, and l is the length of the nanopillar. The optimum thickness will, then, be the one such that the total light absorbed across the solar spectrum is greater than 90% according to the relation

$$A = 1 - \frac{I}{I_0} = 1 - e^{-\propto l} \tag{1.9}$$

where A is the percentage of light absorbed at a specific wavelength. The optimum width of each pillar is 2x the exciton diffusion length, L_D, so that the shortest path to the donor-acceptor interface is 1 diffusion length for each exciton. Returning to the idea of extending the absorption range, a simple method of achieving this is mixing multiple donor materials together with complementary absorption. These donor materials must have compatible deposition techniques, but, more importantly, have the appropriate energy levels to allow for charge drift in the right direction. In other words, their LUMO's (lowest unoccupied molecular orbitals) and HOMO's (highest occupied molecular orbitals) must be staggered to allow for electrons to cascade down towards the cathode and holes cascade upwards towards the anode.

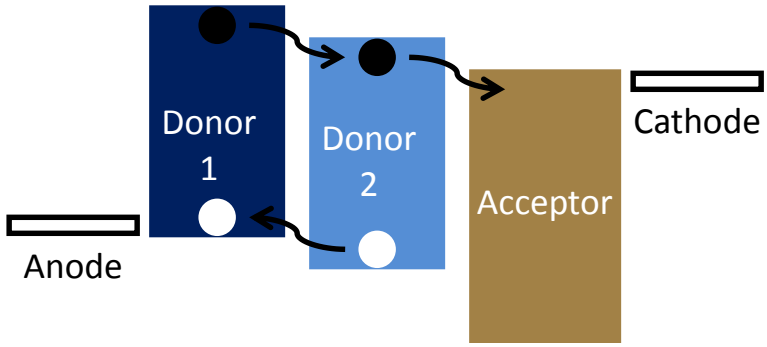

Fig. 9 Schematic showing the appropriate relative energy levels of multiple donors, the acceptor, cathode, and anode.

Before the active films are structured by nanoimprint lithography, the dimensions of the template must be determined. Using pores that generate cylinders with diameter twice the exciton diffusion length is a good rough guide. For this reason, first the exciton diffusion length must be measured with a routine technique. Two separate samples are made to assist the measurement. One is an optically thick film of the donor material on glass with a blocking layer on top (i.e. bathocuproine, BCP). The other is another optically thick donor film on glass with a quenching layer on top (i.e. C60). When light is shone on the former structure, excitons do not have an interface at which to split and, therefore, recombine. The light emitted upon recombination is observed by a photoluminescence measurement. In the latter sample, many excitons, depending on the exciton diffusion length, can reach the interface and be split. Consequently, there will be less photoluminescence. Since the amount of photoluminescence is related to how well excitons diffuse to the interface with the quenching layer, a photoluminescence measurement can be used to determine the exciton diffusion length. The difference in photoluminescence for these two samples will be evident. The ratio of the photoluminescence of the blocked sample, η_b, to the quenched sample, η_q, is related to the exciton diffusion length by the following expression:

$$\frac{\eta_B}{\eta_Q} = \alpha(\lambda) * L_D + 1. \qquad (1.10)$$

Thus, on a plot of $\frac{\eta_B}{\eta_Q}$ vs. α(λ), the slope will the L_D.

a)

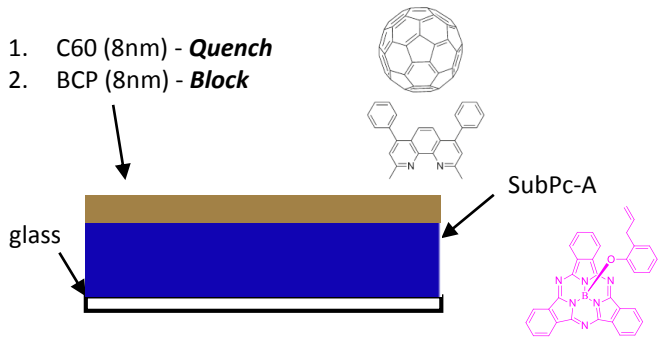

Figure 10 a) Diagram of structure designed to promote exciton photoluminescence (blocked version) and another designed to promote exciton quenching (quenched). b) Schematic of plot showing photoluminescence of both blocked (blue) and quenched (red) samples. c) Schematic of the plot of the ratio of the photoluminescence of the blocked sample to that of the quenched sample versus excitation wavelength

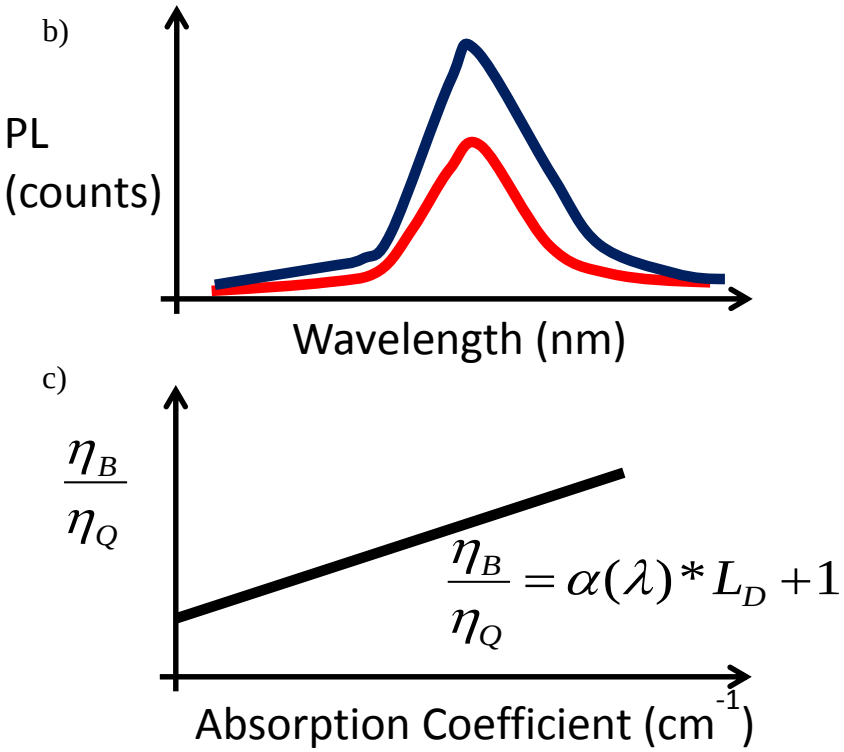

2.3 Materials and Instrumentation

SubPc-A was prepared and characterized according to previous reports.[17] An absorption spectrum of thin films was measured with a CARY 5000 UV-Vis-NIR spectrophotometer. Cyclic voltammetry was performed with a Solartron 1285 potentiostat with a scan rate of 100 m•V s^{-1}, wherein a silver wire acts as the reference electrode, glassy carbon as the working electrode, a platinum wire acts as the counter electrode. Samples were prepared in dichloromethane solution with 0.1M tetrabutylammoniumhexafluorophosphate as the electrolyte and ferrocene as an internal standard. The thickness of films was measured using a Horiba Uvisel Spectroscopic Ellipsometer. Photoluminescence was measured using a Nanolog spectrofluorometer.

2.4 Materials Characterization

The first interface to be manipulated is the donor-acceptor interface. If the donor can be made thicker, to absorb more light, charge transport to the donor-acceptor interface can still be efficient if the donor is nanostructured. For this reason, several solution-processable molecular donors were selected for their very special properties to be patterned. 2-Allylphenoxy-(Subpthalocyaninato)boron (III) has excellent attributes for a photovoltaic device: high solubility, low tendency to aggregate, and high extinction coefficient. For these reasons it is possible to deposit high quality films in comparison to many other solution processed films for which the material may aggregate or have poor solubility. These properties emerge from the structure of the SubPc-A molecule, which is non-planar and pyramidal. It has already been employed in a bilayer solar cell by Ma *et. al.*, inspired by work in 2009 that pushed the

efficiency of solution processed molecular solar cells from 1.3% to 3%. A 20nm thick SubPc-A layer in conjunction with 32nm of the acceptor C60 converted power at a 1.7% efficiency.[17]

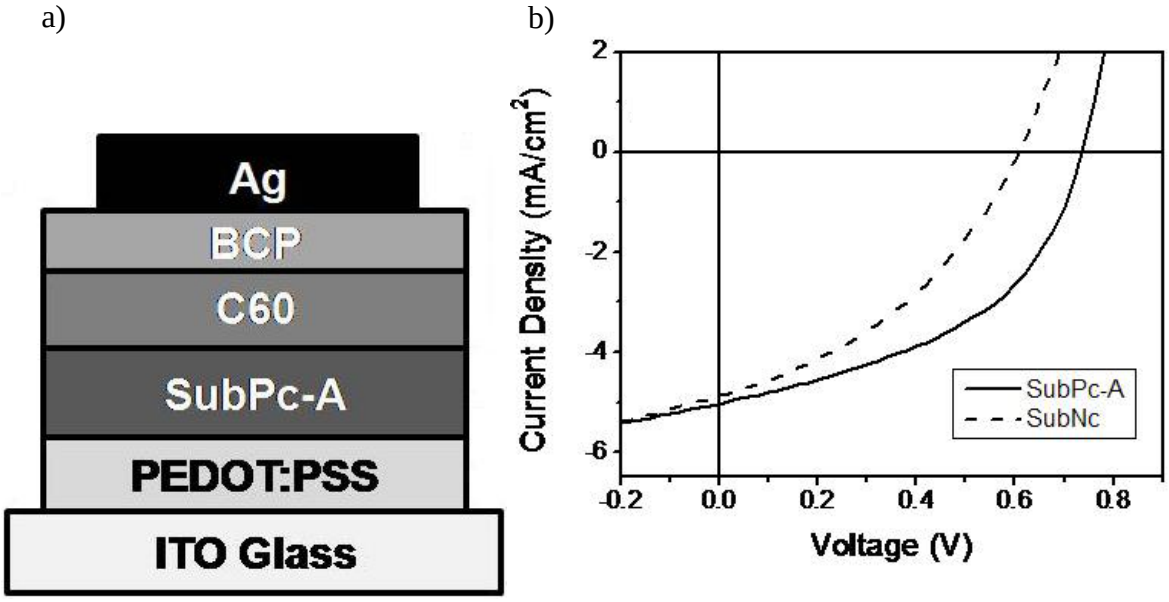

Figure 11 a) Diagram of the structure of the bilayer solar cell constructed with ITO/PEDOT:PSS (30nm)/SubPc-A(20nm)/C60(32nm)/BCP(10nm)/Ag(100nm). b) Plot of the IV behavior of a bilayer solar cell with a SubPc-A donor (solid) and a subnapthalocyanine, SubNC (dashed).[17]

2, 4-bis[4-(N,N-diisobutylamino)-2,6-dihydroxyphenyl]squaraine (SQ, Fig. 12) is another interesting soluble small molecule due to its high absorption, albeit in the fairly narrow range of 600nm-700nm.[19] Squaraine dyes, reported by Triebs in 1965, are squaric acid derivatives characterized by a C_4O_2 cyclobutadione bridge with an electron-deficient Hückel ring. As such, the four membered ring acts as an acceptor and it is surrounded by two electron-donating groups in a donor-acceptor-donor (D-A-D) structure. Many of the derivatives maintain the Hückel ring, but exchange the donor moieties to achieve different optical properties. The particular derivative employed here has been shown to exhibit excellent film quality, though the solubility is limited. Due to its very small exciton diffusion length, ~2nm, the thickness of the film in the bilayer device is much smaller than typical, 10nm.[20]

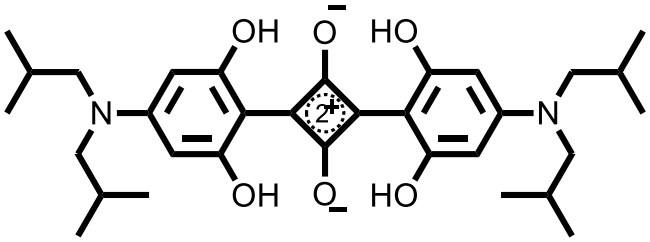

Figure 12 Schematic of the structure of SQ

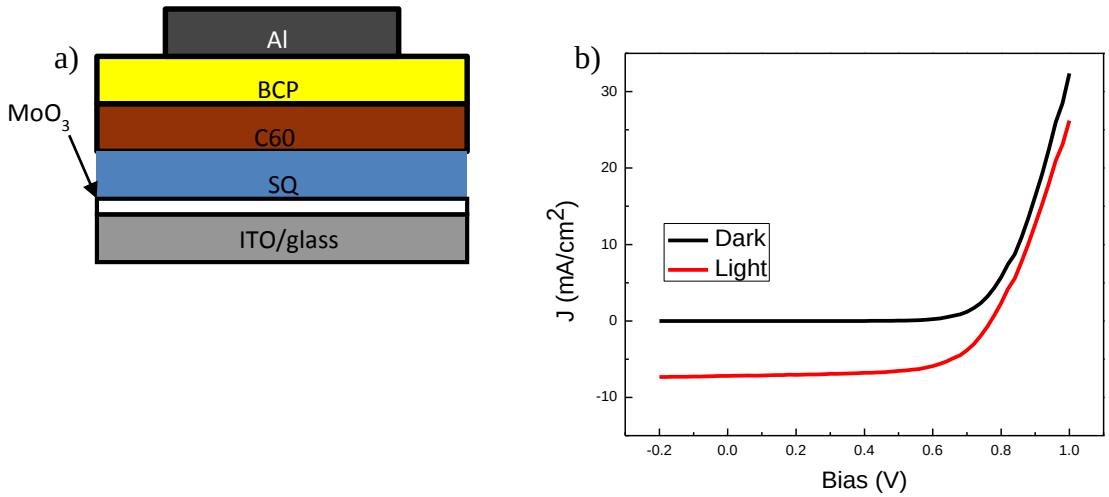

Figure 13 a) Diagram of the structure of the bilayer solar cell constructed with ITO/MoO_3 (8nm)/SQ(10nm)/C60(40nm)/BCP(10nm)/Al(100nm). b) Plot of the IV behavior of a bilayer solar cell with a SQ donor.

The final small molecule studied is the aforementioned BOADPM (Fig. 14), a near-infrared absorber. Like SQ and SubPc-A, BOADPM is amorphous in the as-cast state and has quite a small exciton diffusion length, ~4nm, as estimated by Leblebici.

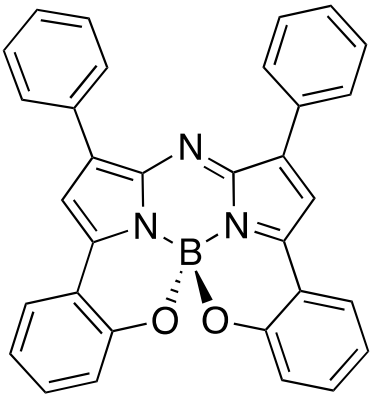

Figure 14 Schematic of the structure of BOADPM.

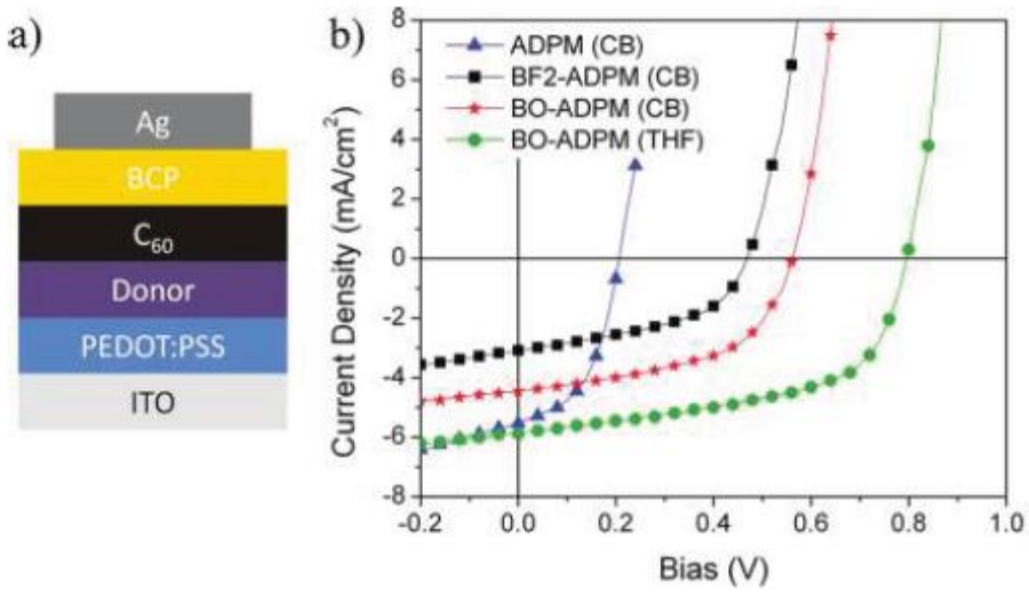

Figure 15 a) Diagram of the structure of the bilayer solar cell constructed with ITO/PEDOT:PSS (30nm)/BOADPM(14nm)/C60(40nm)/BCP(10nm)/Ag(100nm). b) Plot of the IV behavior of a bilayer solar cell with several different azadipyrromethene donor layers.[7]

First nanoimprint lithography was attempted using a single material, SubPc-A. The thermotropic properties of SubPc-A were assessed with thermogravimetric analysis (TGA) and differential scanning calorimetry (DSC). TGA revealed the decomposition temperature to be roughly 280°C while DSC pointed to a T_g at 96°C (Figs. 16 and 17). In light of this information, a temperature of 200°C and pressure of 200 Pa was chosen to conduct the nanoimprint lithography and found to work.

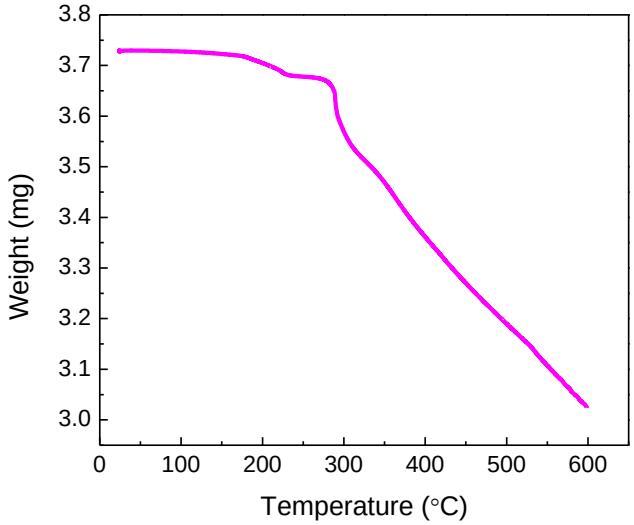

Figure 16 Thermogravimetric analysis of SubPc-A. The scans indicate a decomposition temperature of about 280°C.

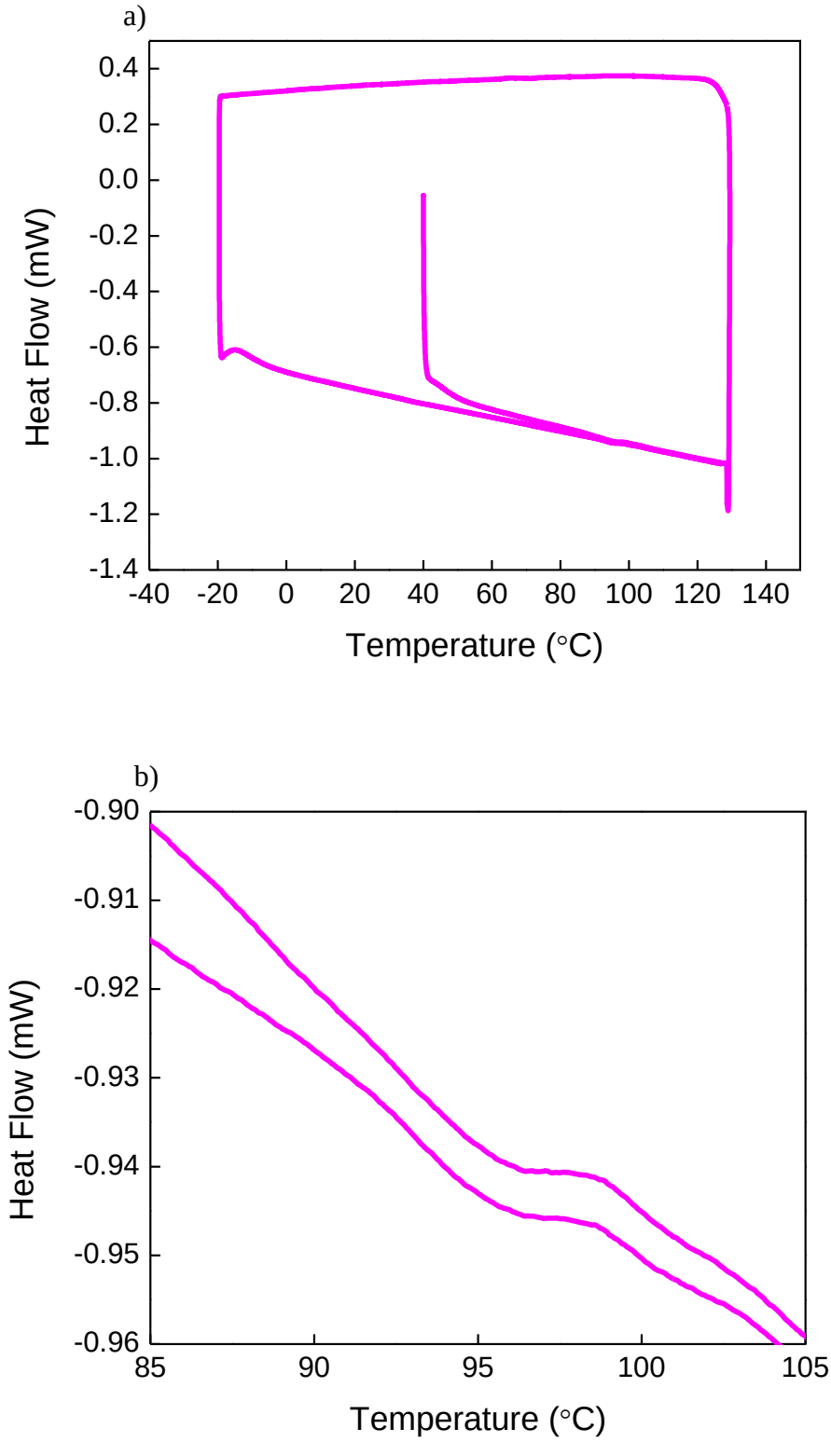

Figure 17 a) Differential scanning calorimetry scan of SubPc-A between -20°C and 130°C b) Zoomed-in view of the DSC curve to highlight the T_g of roughly 96°C.

The thermotropic properties of SubPc-A make it attractive for nanoimprinting. Furthermore, the energy levels are compatible with fabrication of a solar cell with the structure Al/BCP/C60/SubPc-A/MoO_3/ITO/glass (Fig. 20). These energy levels were calculated using a combination of cyclic voltammetry and UV-Vis spectrometry. First, cyclic voltammetry was used to determine the HOMO relative to an internal ferrocene standard; it came to -5.4eV. The HOMO-LUMO gap was calculated based on the absorption onset at about 600nm = 2eV. This HOMO-LUMO gap was subtracted from the HOMO level to set the LUMO level at -3.4 eV.

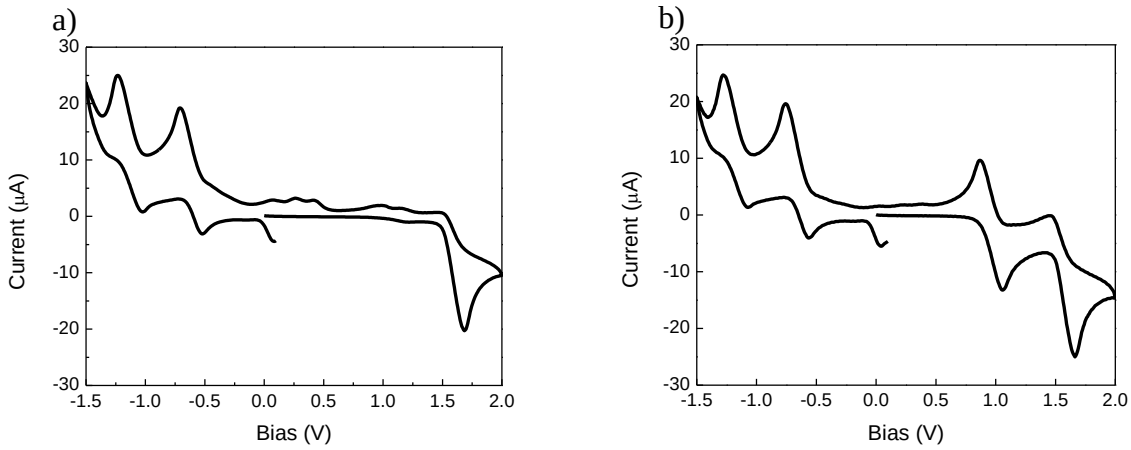

Figure 18 a) Cyclic voltammogram of SubPc-A. b) Cyclic voltammogram of SubPc-A with internal ferrocene standard.

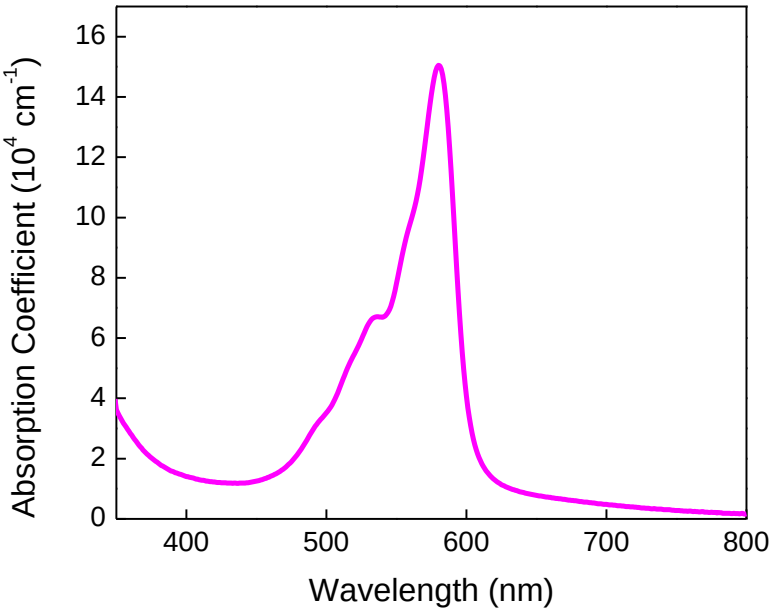

Figure 19 Absorption spectrum of a thin film of SubPc-A.

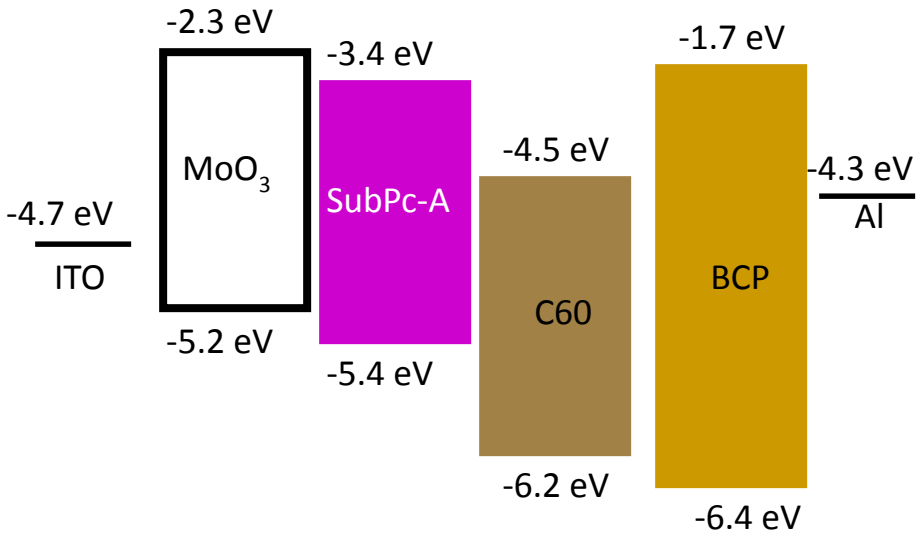

Figure 20 Energy level diagram of a solar cell with structure Al/BCP(8nm)/C60(40nm)/ SubPc-A(29nm)/MoO_3(8nm)/ITO.

SubPc-A was chosen as the best candidate for imprinting both for its absorption in the visible and it processing compatibility. Moreover, because these materials can be dissolved in many of the same solvents, SubPc-A can also serve as a host matrix for a second material to extend the absorption range in a multicomponent donor system.

2.5 Choice of Pillar Dimensions

In order to determining the ideal pillar height, the absorption coefficient at every wavelength was used in conjunction with the solar spectrum (AM1.5) to calculate the thickness at which 90% of incident sunlight would be absorbed. Because of the limited absorption range of SubPc-A, a thickness of approximately 1µm is required to absorb 90% of the light between 400nm and 800nm.

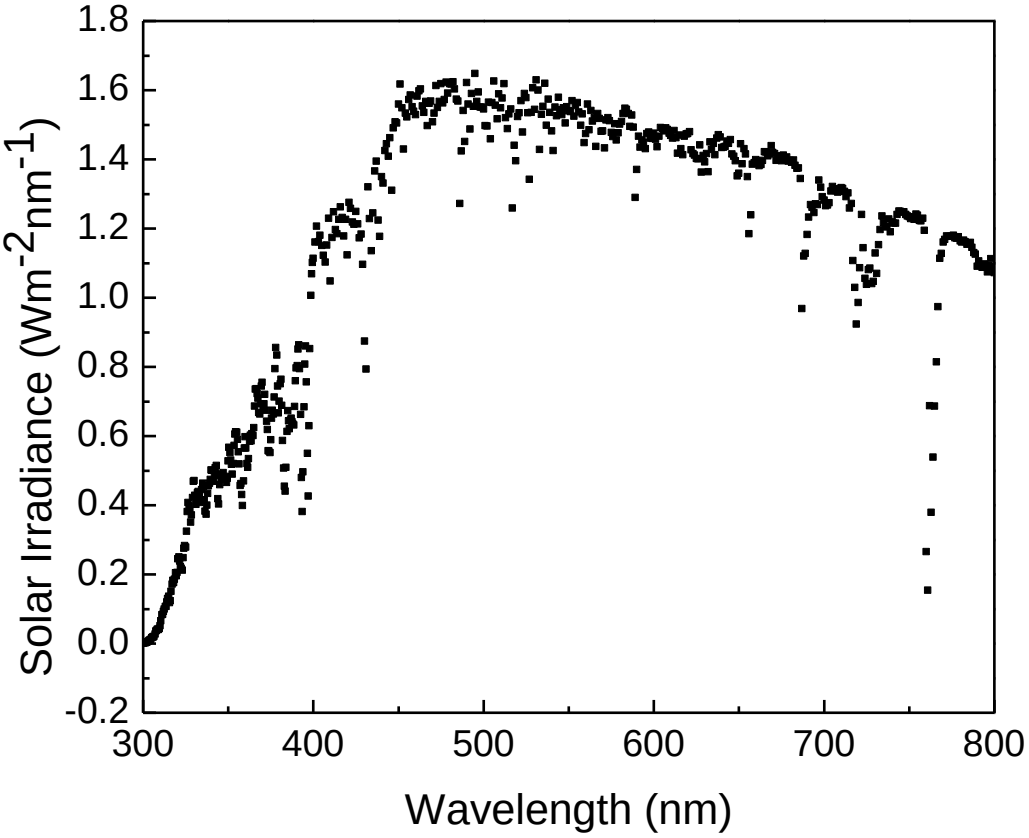

Figure 21 AM1.5 Solar spectrum between 300nm and 800nm.

The ideal pillar diameter was calculated with knowledge of the exciton diffusion length. Two samples were constructed: one with the structure C60(8nm)/SubPc-A(317nm)/glass and the other with the structure BCP(8nm)/SubPc-A(317nm)/glass (Fig. 22). The former structure allowed the excitons generated under illumination to be quenched at the C60/SubPc-A interface while the excitons in the latter structure would recombine and photoluminesce much more readily. At 317nm thick, the SubPc-A layer absorbs about 52% of the incident light between 400nm and 800nm.

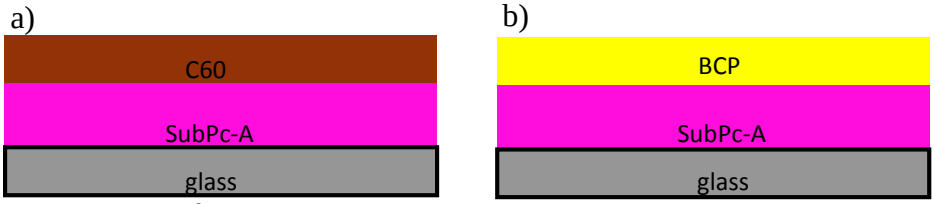

Figure 22 a) Structure of device built to allow exciton quenching at the SubPc-A/C60 interface (C60/SubPc-A/glass). b) structure of device built to allow exciton recombination and photoluminescence due to the blocking effect of BCP (BCP/SubPc-A/glass)

450nm and 600nm, where SubPc-A absorbs, and the photoluminescence was detected. Though there are several techniques[21,22] for measuring the exciton diffusion length of optically thick films, spectrally resolved photoluminescence quenching is the most highly favored for many reasons. The excitons generated by incident light will be distributed throughout the film according to the absorption coefficient, but most will be located near the window. Those excitons that are close to the quenching interface, within a distance of ~L_D, will decay rather than photoluminesce. Therefore, there will be a difference between the photoluminescence efficiency of the blocked layer, η_B, and that of the quenched layer, η_Q. By calculating the ratio $\frac{\eta_B}{\eta_Q}$, systematic errors such as uncertainty in the lamp intensity or variation in exciton generation from sample to sample can be eliminated.[23]

2.6 Results and Discussion

The plot of $\frac{\eta_B}{\eta_Q}$ vs. α(λ) can be fit with the following relationship:

$$\frac{\eta_B}{\eta_Q} = 1.76 + 2 \cdot 10^{-6} * \alpha(\lambda) \qquad (1.11)$$

The coefficient, $2 \cdot 10^{-6}$, corresponds to the exciton diffusion length (L_D) in units of cm so L_D = 20nm, in agreement with literature reported values.[23]

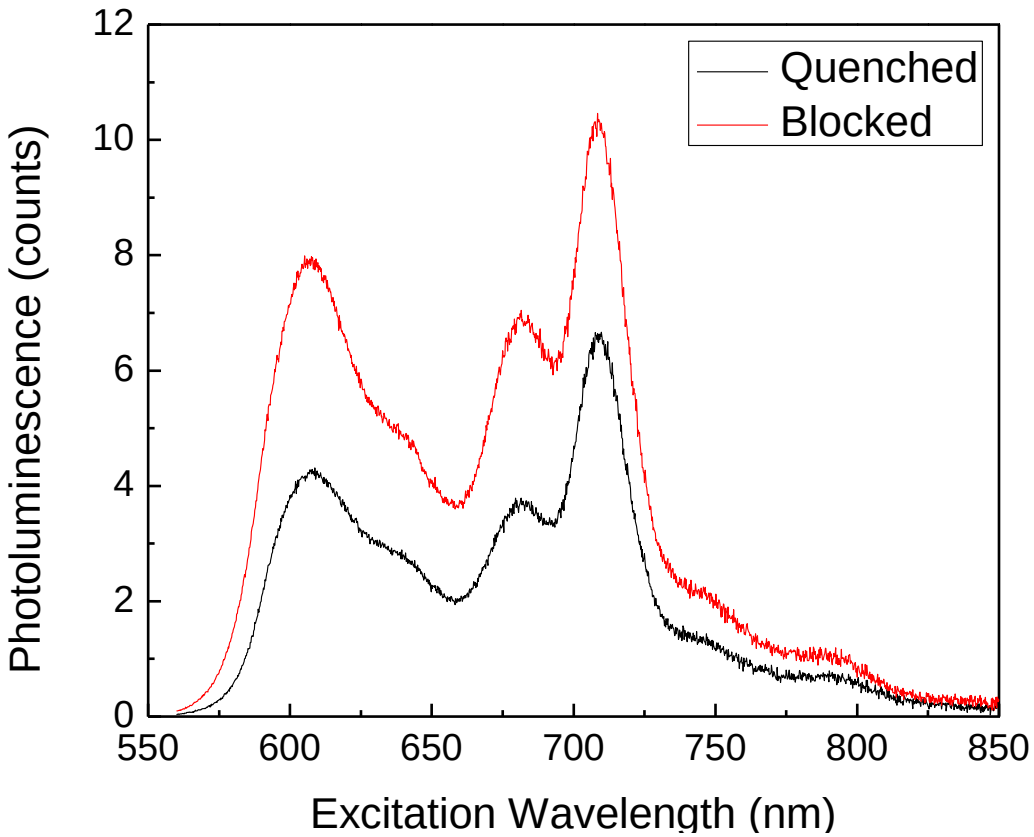

Figure 23 Photoluminescence spectra of quenched and blocked SubPc-A layer at excitation wavelengths between 560nm and 850nm.

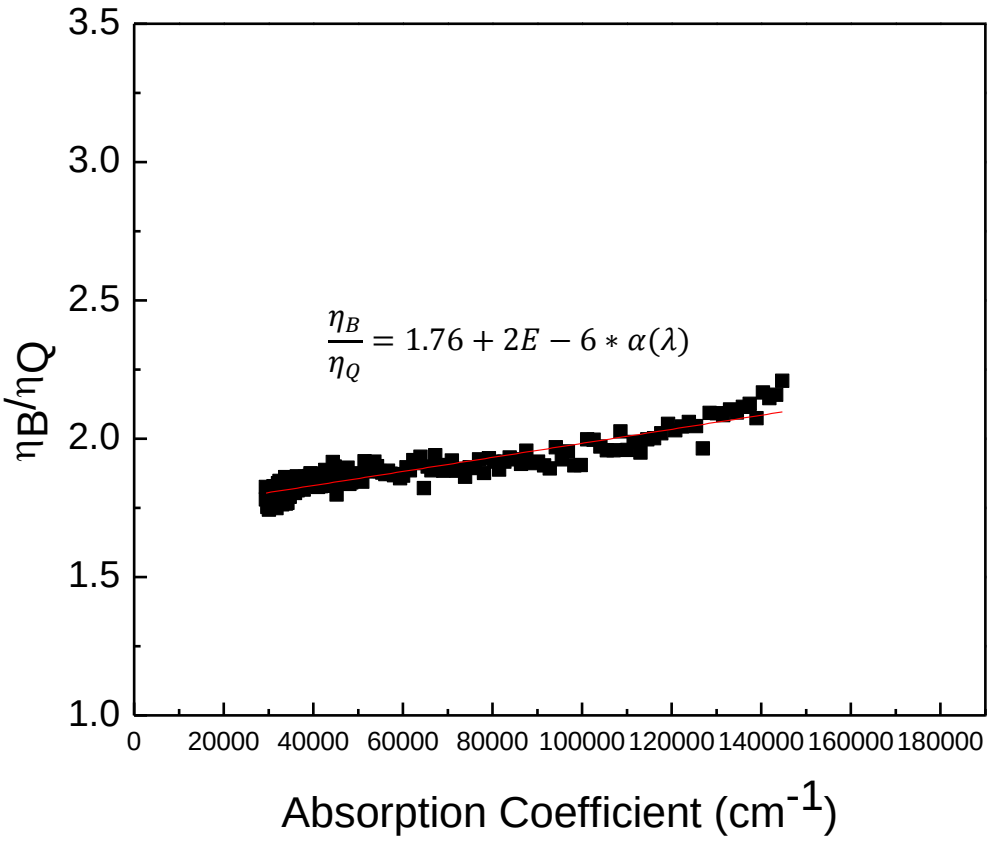

Figure 24 Plot showing the ratio of photoluminescence in the blocked SubPc-A sample to that of the quenched SubPc-A sample versus the absorption coefficient at the excitation wavelength. The slope of the scatterplot corresponds to an L_D = 20nm.

In light of the fact that L_D= 20nm for SubPc-A, the nanopillar diameter should be no more than twice L_D, or 40nm.

When fabricating the silicon template to pattern the desired features, practical engineering concerns arose that called for compromise with the theoretically ideal dimensions. The block copolymer polystyrene-polyethylene oxide (PS-PEO), M_n = 32-b-11 kg/mol, has proven capable of generating domains of PEO with diameter ~20nm (Fig. 25) within the host matrix of PS after being solvent annealed in water and tetrahydrofuran, THF. After solvent annealing, the PEO is largely on the film surface while a portion remains in the nanohole, chemically attached to the PS. Etching for 10s in oxygen plasma removed the PEO to prepare it for the selective SF_6/O_2cryo-ICP etch to form pores within Si. This cryo-ICP etch has a polymer:silicon selectivity of 1:10. Finally, before imprinting, the surface was coated with the release agent 1H,1H,2H,2H-perfluorooctyltrichlorosilane by evaporation.

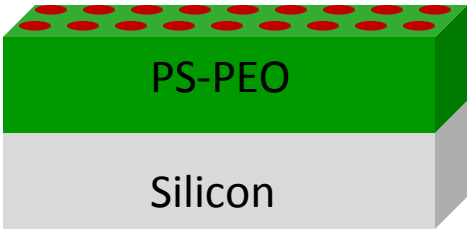

Fig. 25 Schematic of PEO domains (red) in a PS matrix (green) on top of a silicon substrate.

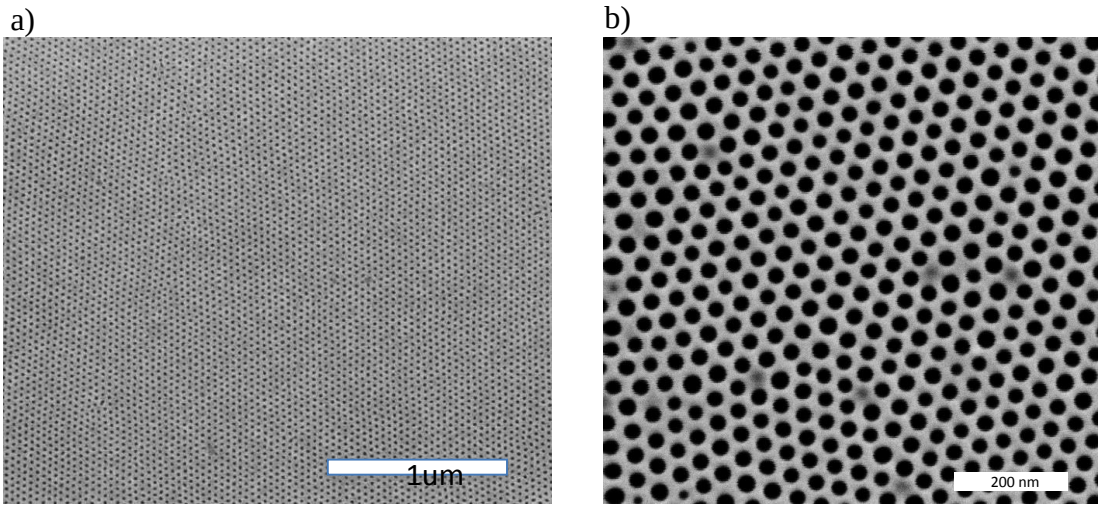

Fig. 26 a) The PS-PEO (32-11k) mold deposited on a silicon wafer. b) Silicon wafer after it has been etched to generate nanopores.

The release agent helps to ensure clean pattern transfer, as there can be a number of imperfections otherwise (Fig. 27). Another practical consideration is that if the diameter of the pillars is only 20nm, the height should be roughly the same height for structural integrity; taller pillars are more easily damaged during the mold release. For this reason, the mold was etched to a depth of roughly 40nm, ensuring that the pillars formed would be no taller than that height depending on the initial layer thickness before imprinting.

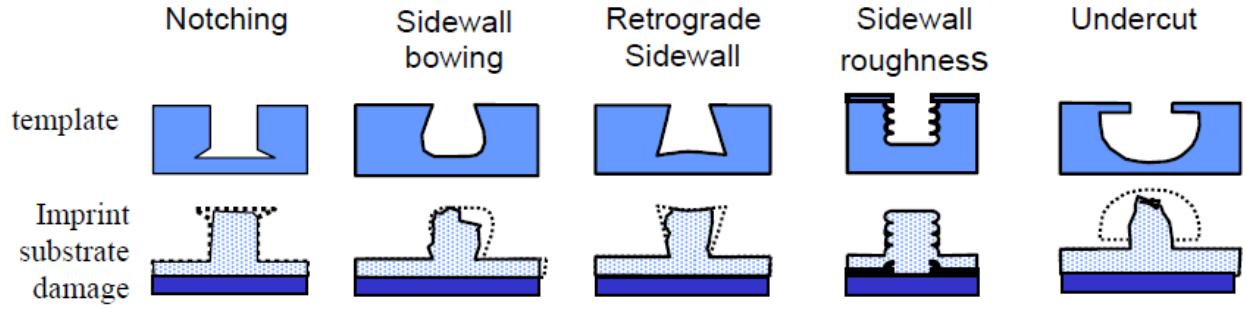

Fig. 27 List of common issues arising from imperfect pattern transfer from a hard template to a soft organic layer.[24]

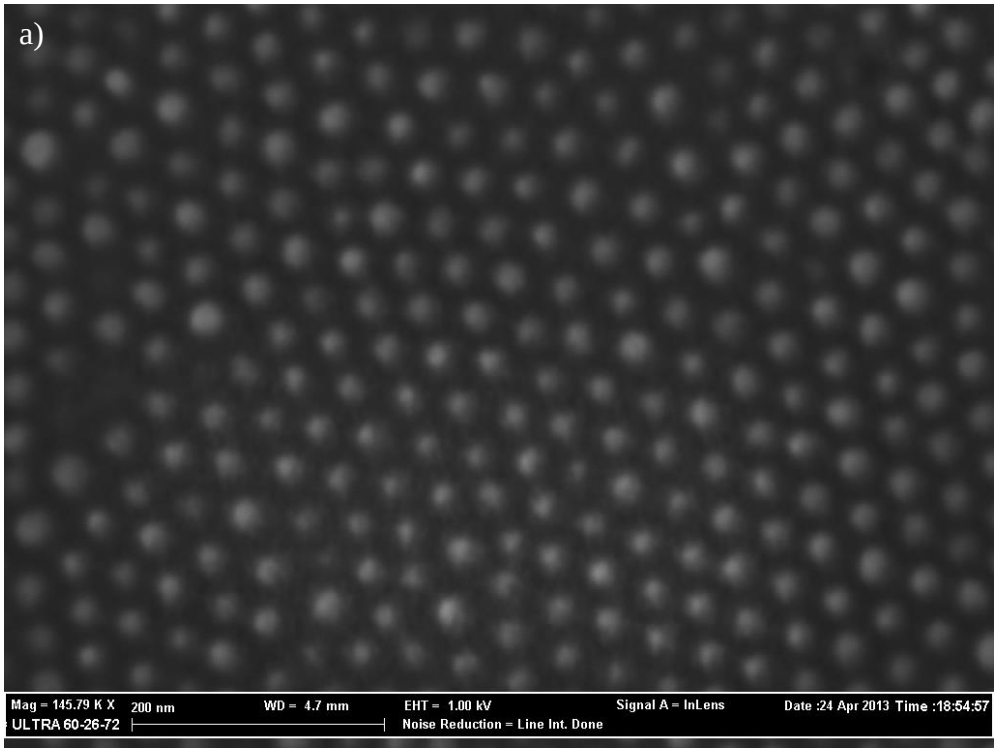

Fig. 28 a) SEM image of a nanoimprinted SubPc-A film with features of approximately 20nm in diameter. b) an SEM image from the same sample at a different location with a higher number of defects.

A thin layer of SubPc-A, 29nm thick, was deposited on silicon slide (2cm•2cm) to be imprinted as a proof of concept. While in some areas of the slide, there was good pattern transfer (Fig. 28 a), in other areas there were many defects (Fig. 28 b). The defects are most likely due to an unclean template in which some of the pores may have clogged with organic material from previous imprints. While the concept was proven, the demonstration does point to a difficulty in ensuring good pattern transfer over area large enough to construct a device (~ .03 cm^2).

Chapter 3

Nanostructuring of a Multi-Component Donor

3.1 Choice of Materials

Additional materials have been identified to be used in conjunction with SubPc-A to extend the absorption range of the donor layer by making a two-component mixture. Both SQ and BOADPM are near infrared absorbers and their absorption ranges are complementary (Fig. 29). The fact that they are miscible in many of the same solvents makes them an ideal set of materials from which to choose two for a two-component mixture. Because SQ has both the highest maximum absorption coefficient and the most limited solubility, it can serve as the minority component in a matrix of either SubPc-A or BOADPM.

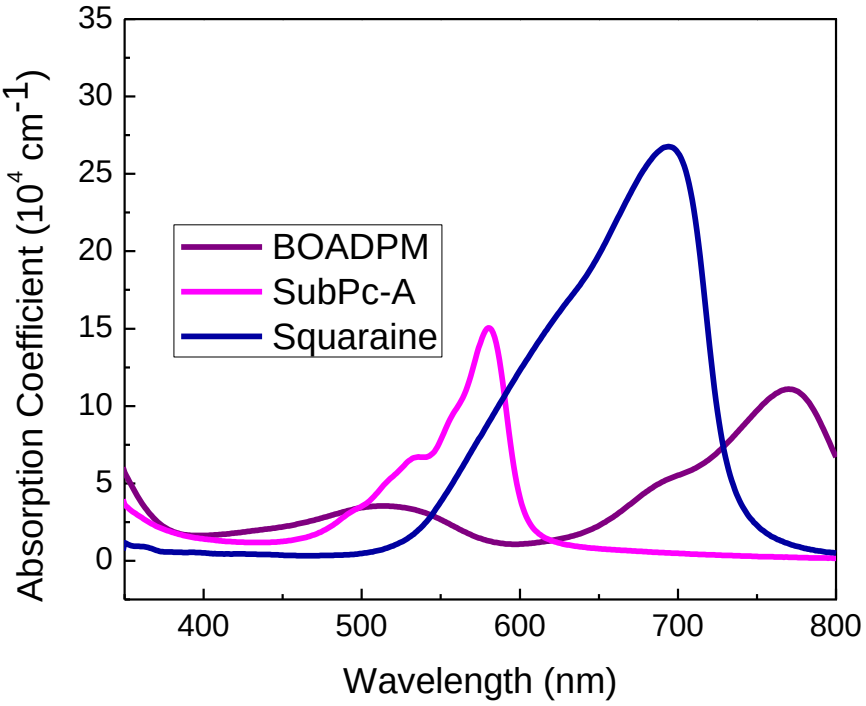

Figure 29 Plot of the absorption coefficient for the candidate donor materials: BOADPM, SubPc-A, and SQ.

Moreover, the energy levels of SQ and BOADPM show that there is promise to construct a device of the structure Al/BCP/C60/SubPc-A/SQ or BOADPM/MoO_3/ITO/glass. While the energy levels of BOADPM have been previously determined by Leblebici *et. al.*, those for SQ were calculated using CV in conjunction with UV-Vis spectroscopy (Fig. 30).

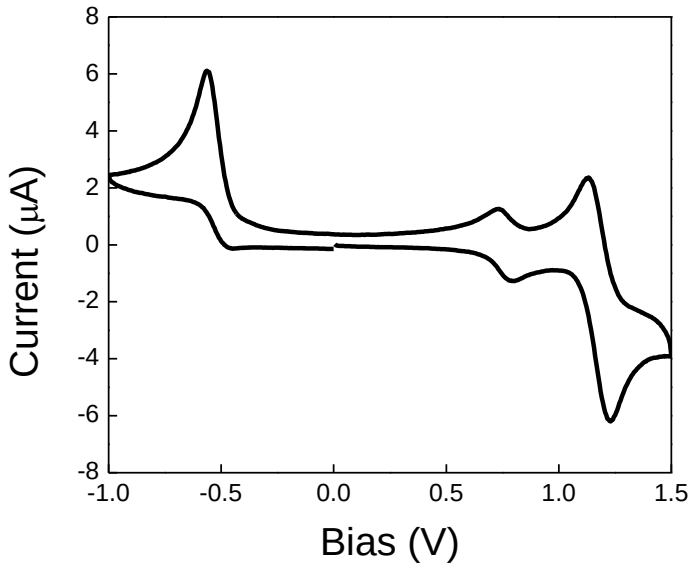

Figure 30 – Cyclic voltammogram of SQ with internal ferrocene standard. The oxidation peaks of the ferrocene standard are shown at ~.7V and .74V while those of SQ are at ~1.2V and 1.25V.

Based on these results, a band diagram of materials to be potentially used together can be constructed showing that donor combinations of SQ/BOADPM and SubPc-A/BOADPM can be promising.

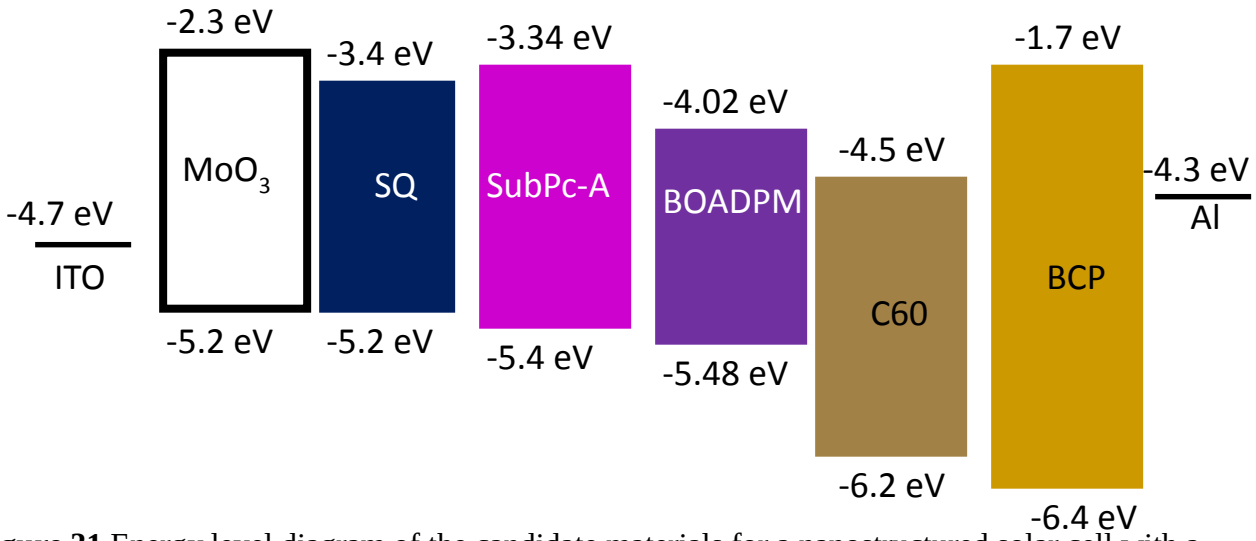

Figure 31 Energy level diagram of the candidate materials for a nanostructured solar cell with a multi-component donor.

3.2 Results and Discussion

The thermotropic properties of SQ and BOADPM were assessed to determine compatibility with nanoimprint lithography. It was observed that SQ and BOADPM do not decompose until a temperature of 360°C and 290°C, respectively (Fig. 32).

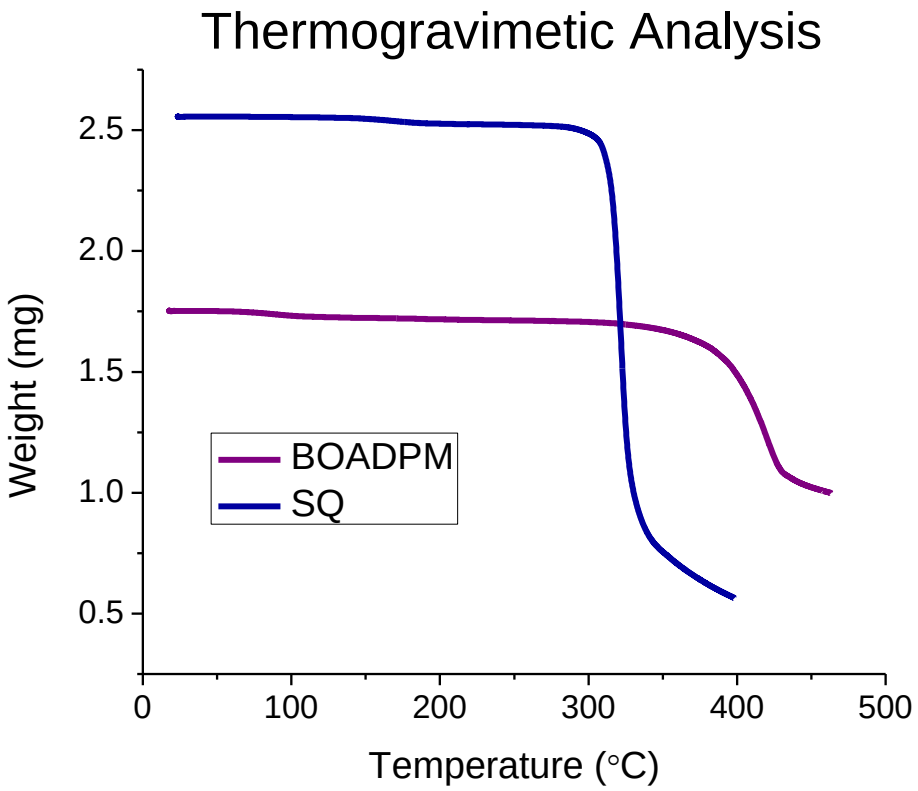

Figure 32 Thermogravimetric analysis of BOADPM and SQ, showing decomposition temperatures at roughly 360°C and 290°C, respectively.

Differential scanning calorimetry identified T_g at 96°C for SQ and 150°C for BOADPM. T_g for SQ was revealed as a step in the DSC curve (Fig. 33), similar to that of SubPc-A, while that of BOADPM (Fig. 34) was revealed as two humps in the plot which indicated a glass transition (endothermic) and recrystallization (exothermic). The concave up hump at ~160°C indicates that the material is taking up heat to transition to the glassy, rubbery state while the concave down hump at 180°C indicates that the material is releasing heat as it recrystallizes. Because the decomposition temperature is so high relative to the glass transition temperature for each molecule, there is a large temperature window in which to complete the nanoimprint lithography.

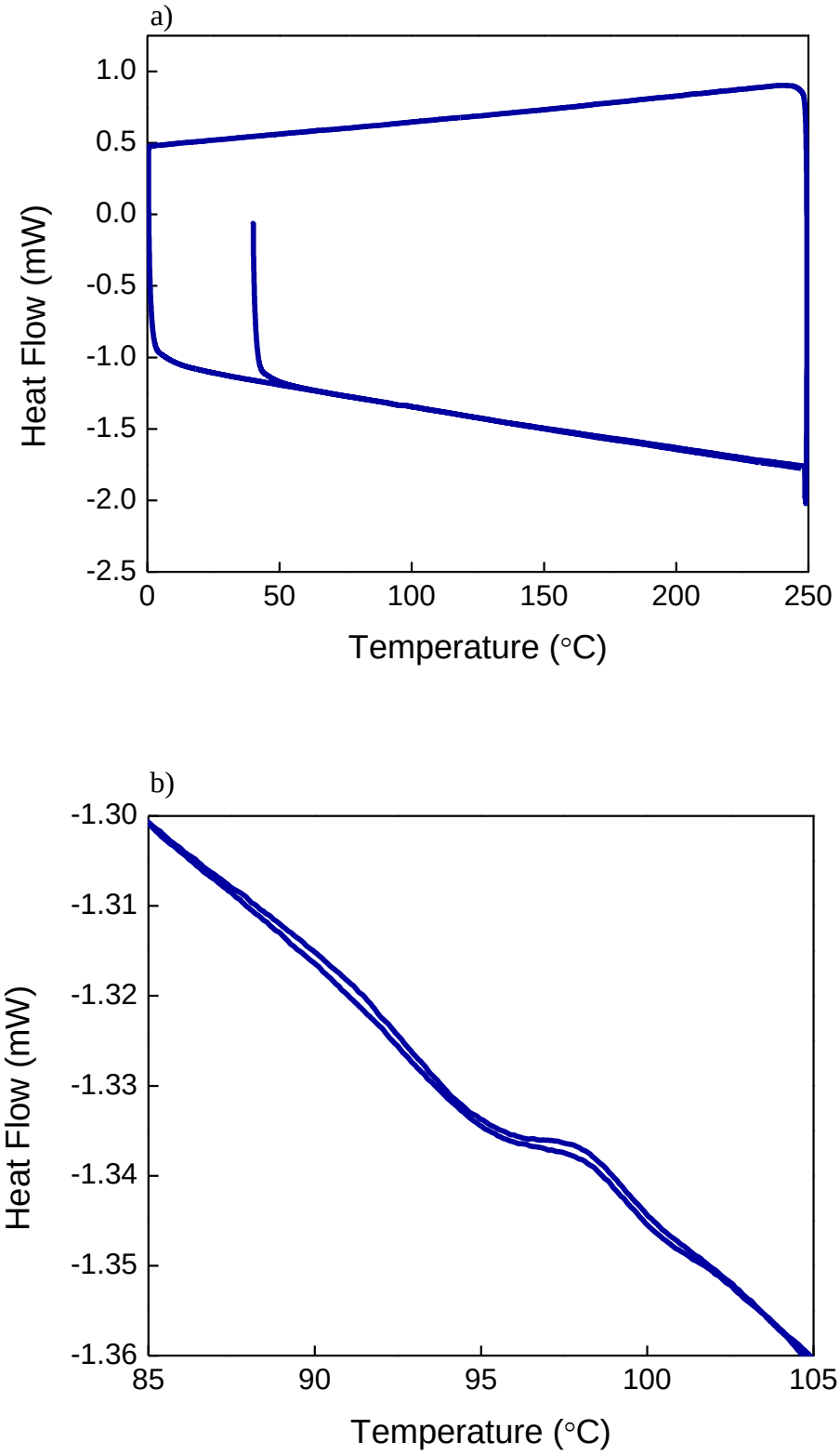

Figure 33 a) Differential scanning calorimetry scan of SQ between -20°C and 130°C. b) zoomed-in view of the DSC curve to highlight the T_g of roughly 96°C.

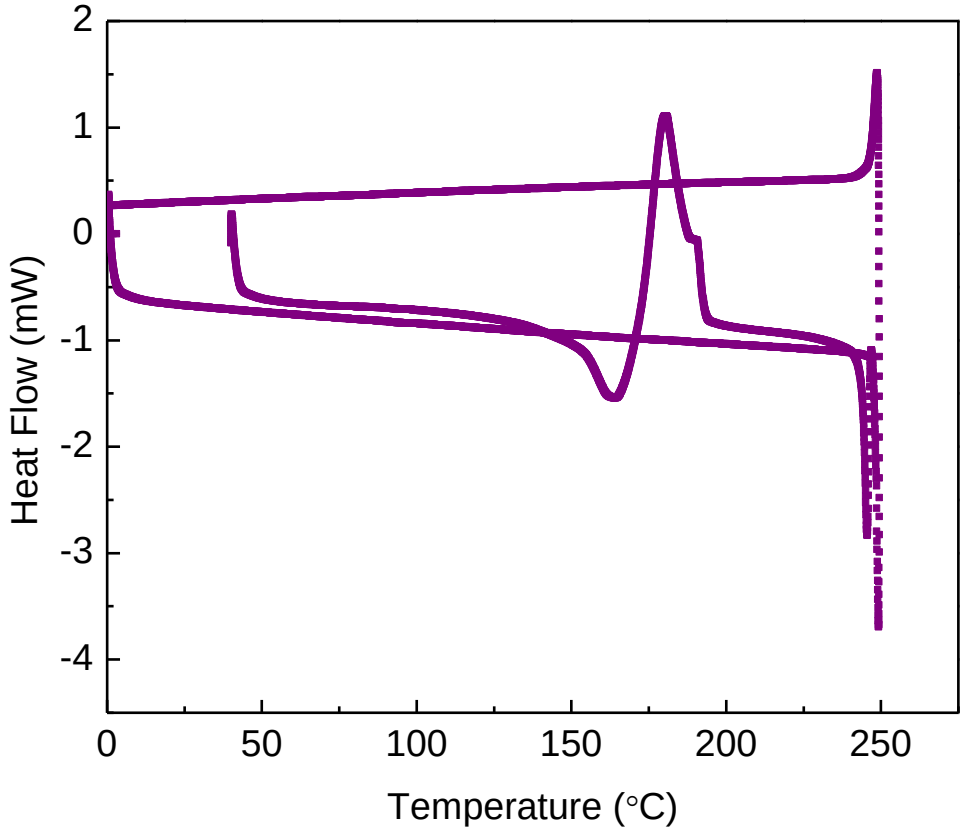

Figure 34 Differential scanning calorimetry scan of SubPc-A between -20°C and 130°C indicating a T_g of roughly 150°C.

Nanoimprint lithography was conducted using BOADPM to confirm that it could also be used as a matrix material like SubPc-A.

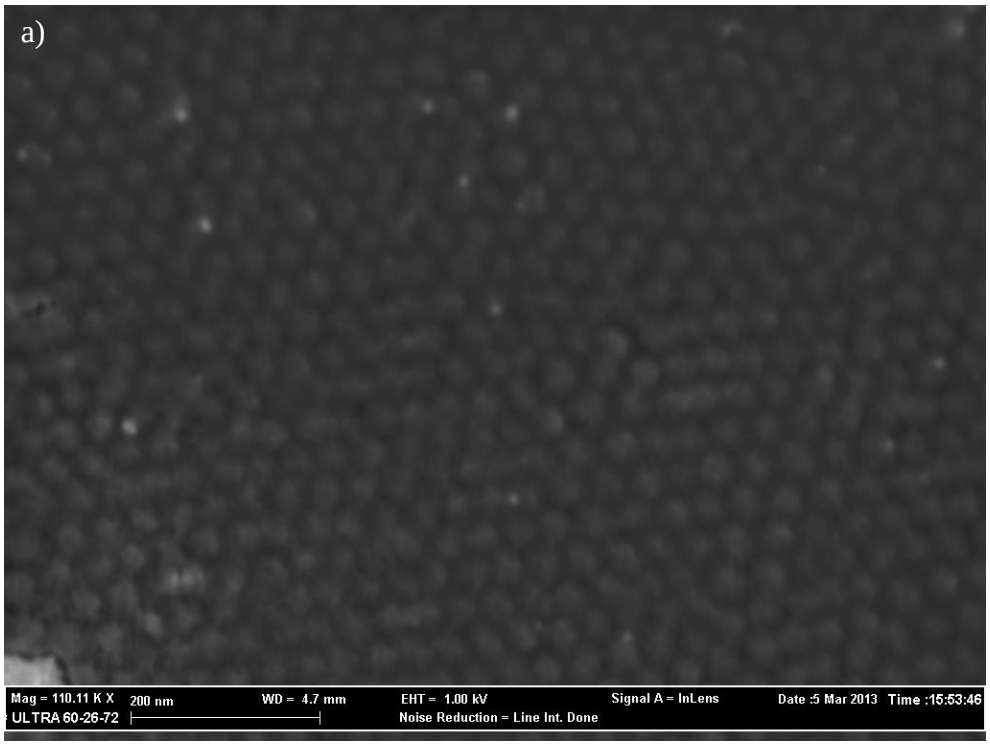

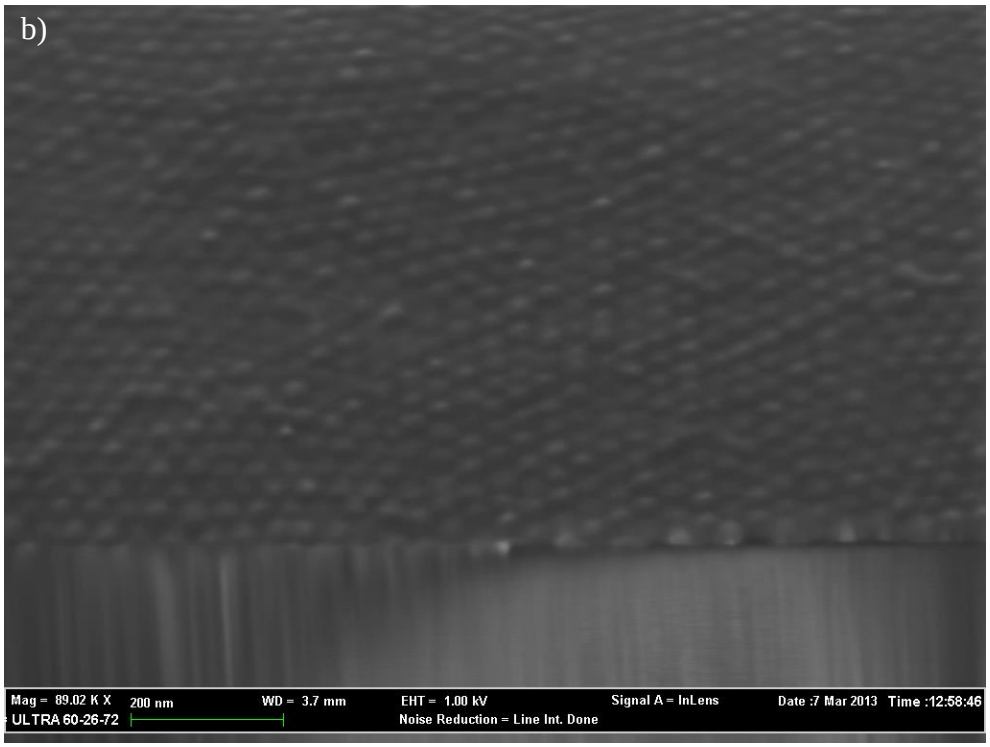

Fig. 35 a) Top down SEM view of nanimprinted BOADPM on Si and b) tilted SEM view of BOADPM showing nanopillars roughly 20nm in diameter and height.

Chapter 4

Anode Surface Engineering with a Hole Injection Layer

4.1 Introduction to Electrode Modification

Recently, interfaces between materials in organic solar cells have garnered much attention in pursuit of highly efficient and stable devices and modules.[25-56] One of the critical components of OSCs is the interfacial layer between the photoactive layer and electrodes. A desirable interfacial layer has several important properties, including the ability to 1) enhance the compatibility of the electrodes and organic active layers, 2) adjust the energy barriers for efficient charge collection, 3) form a preferential contact for one kind of carrier, 4) preclude chemical or physical interactions between the electrodes and photoactive layers, and 5) serve as an optical spacer. A plethora of p- and n-type interface materials have been studied, including salts, self-assembled organic monolayers, metal oxides, graphene oxides, and doped conductive polymers. Poly(3,4-ethylenedioxythiophene):poly(styrenesulfonate) (PEDOT:PSS) has been one of the most commonly used hole-selective interfacial materials, providing a smooth anode surface, reducing the leakage current, and enhancing device stability compared to a pristine electrode.[57] However, it is not an ideal hole selective layer due to several issues: its intrinsic acidity and hygroscopicity leads to sacrifices in device stability and degradation, and its low LUMO level and bandgap result in poor electron blocking and strong exciton quenching. Both inorganic and organic interfacial layers have been tested to replace the problematic PEDOT:PSS. $CsCO_3$, and V_2O_5, NiO, and graphene oxide are among the inorganic hole-selective compounds that have been deposited on ITO with the intention of improving each of the important photovoltaic figures of merit, short circuit current (J_{sc}), open circuit voltage (V_{oc}), and fill factor (FF). Organic semiconductors such as tris[4-(5-phenylthiophen-2-yl)phenyl]amine (TPTPA), 4,4',4"-tris[N-(3-methylphenyl)-N-phenylamino]triphenylamine (MTDATA), and dithiapyrannylidenes (DITPY) have been employed recently, as well. Furthermore, the organic-inorganic interface has been modified with interfacial dipoles to alter the relative energy levels of the organic and inorganic components. Traditionally, ITO is still used as the bottom electrode since it can conduct holes and electrons, so an electron selective layer must be deposited on the ITO surface. Though generally believed to be less cost-efficient than solution processing, high vacuum processing has been the method of deposition for most of these materials. To our best knowledge, little has been reported on OSCs with solution processed p-type organic interface materials, especially small molecules. Herein is a study on two p-type triindoles, triazatruxene (TAT) and N-trimethyltriindole (TMTI), as solution processable hole-selective materials for use in OSCs with bilayer and inverted structures. Owing to their unique discotic π-extended aromatic structure, these *C3* symmetric fused carbazoletrimers and their derivatives are characterized by attractive physical and electronic properties for organic electronic devices, e.g. liquid

crystallinity, strong fluorescence, and high carrier mobility. In addition to these properties, our investigation of TAT and TMTI as hole-selective materials is also motivated by their facile preparation, electrode compatibility, high solubility, wide bandgap with good transparency in the visible region, high LUMO energy level, and low HOMO level.

4.2 Materials and Instrumentation

Triazatruxene (TAT) and N-trimethyltriindole (TMTI) were synthesized and purified following the widely reported procedures in the literature.[70] Pre-patterned ITO-coated glass substrates were supplied by Thin Film Devices Inc. Poly(3-hexylthiophene) (P3HT) was supplied by Rieke Metals, Inc. Phenyl-C61-butyric acid methyl ester (PCBM) was supplied by Nano-C Inc. Sublimed grade C60 and Bathocuproine (BCP) were supplied by Aldrich. PEDOT:PSS (Baytron PH 500) was supplied by H.C.Starck.

The thickness of these films was determined with a Dektak 150 profilometer. In order to investigate the electronic properties of the materials, density functional theory (DFT) calculations were performed with the Spartan'08 software package using the B3LYP hybrid functional and the 6-31*G basis set. The orbital energy levels in vacuum, minimum energy conformations, and electron density plots are mapped.

4.3 Device Fabrication and Testing

Both conventional and inverted photovoltaic devices were fabricated. The planar heterojunction (bilayer) solar cells were constructed with an architecture of ITO/PEDOT:PSS (40 nm)/TAT or TMTI (~23 nm)/C60 (32 nm)/BCP (8 nm)/Ag (100 nm). ITO-coated glass substrates (15 Ω sq^{-1}) were thoroughly cleaned with detergent, deionized water, acetone, and isopropyl alcohol before being dried in an oven at 140 °C for 10 min. Next, substrates were treated with UV-ozone for 10 min and coated with PEDOT:PSS at a spin speed rate of 4000 rpm. The substrates were then baked in an oven at 140°C for 20 min to remove the solvent and transferred into the glove box for the remaining processing steps. TAT and TMTI films were spin-coated from a 4 mg/mL solution in methanol and chlorobenzene, respectively. Both solutions were filtered using a 0.45 um polytetrafluorethylene filter prior to spin coating at 2000 rpm for 40 sec. C60, BCP, and Ag were thermally evaporated under high vacuum (~2×10^{-6}mbar) at rates of 1.5 $Å s^{-1}$, 1.5 $Å s^{-1}$, and 4 $Å s^{-1}$, respectively. The devices were then annealed at 120 °C for 10 min.

For inverted devices, titania was deposited from a sol-gel route onto ITO films. First, ITO substrates were cleaned following the procedure described above. The titania solution was prepared by mixing 200 ml absolute ethanol (Aldrich), 5 ml ultrapure water and 2 ml concentrated HCl (37.5%). I then mixed titanium ethoxide with this solution in a 1:8 ratio. The aforementioned solution of titanium ethoxide diluted in ethanol/water/HCl was spin-coated onto ITO at 2000 rpm to give a film of ~70 nm. The films were annealed at 450 °C for 2 hours to promote the growth of the anatase crystalline phase. These films were subsequently cleaned in the solvents mentioned above before being UV-ozone cleaned again for 10 min. The active layer was spun from a 20 mg mL^{-1} solution of P3HT:PCBM (1:.6 wt%) blend in chlorobenzene at 1000 rpm for 60 sec in a nitrogen-filled glovebox. The TAT layer, which impedes electron flow, was spun from a 2 mg/ml solution (in methanol) at 2000 rpm for 40 sec. All of the above

solutions were passed through a 0.45 µm polytetrafluorethylene filter prior to spin coating. Subsequently, a Au layer (50 nm) was thermally evaporated under high vacuum (~ 2×10^{-6} mbar) at a rate of 2 Å•s^{-1}.

The performance of all devices was measured at room temperature in a nitrogen environment under AM 1.5G solar illumination at 100 mW•cm^{-2} (1 sun) using a Thermal-Oriel 300W solar simulator with filter and a Keithley236 source-measure unit for current density-voltage curves. External quantum efficiency (EQE) was measured with a monochromator and calibrated against a silicon diode.

4.4 Material Properties

UV-Vis-NIR spectroscopy was used to determine the absorption of the solution processed thin films of TAT and TMTI as shown in Figure 37a. The absorption was observed predominantly in the ultraviolet (UV) region for both films, suggesting high optical bandgap with excellent transparency in visible region. Based on the absorption edges, I estimated the optical bandgaps to be ~3.35eV for TAT and ~3.05 eV for TMTI, respectively. Cyclic voltammetry was used to deduce the redox properties and then energy levels of TAT and TMTI. The first oxidation potentials were observed at~ 0.23 V and ~ 0.30 V (relative to ferrocene, - 4.8 eV respect to zero vacuum level)[71] for TAT and TMTI respectively (Figure 37b), which correspond to HOMO levels of -5.03 eV and -5.1 eV. No reduction peaks were observed within the scan range as a result of their electron rich nature. The LUMO levels were estimated based on the optical gaps and HOMO levels, yielding values of -1.68 eV and -2.05 eV for TAT and TMTI respectively. Figure 37 shows the energy levels schematically of these molecules together with others used in our study. We can find that both TAT and TMTI have quite high LUMO levels and modest HOMO levels, which should afford them great electron blocking and hole extracting capabilities. DFT calculations were also executed with results shown in the insert of Figure 37a, exhibiting strong agreement with the experimental results. According to the energy level alignment in Figure 38, little energetic barrier is expected for hole transfer between these molecules and common hole-collective electrodes.

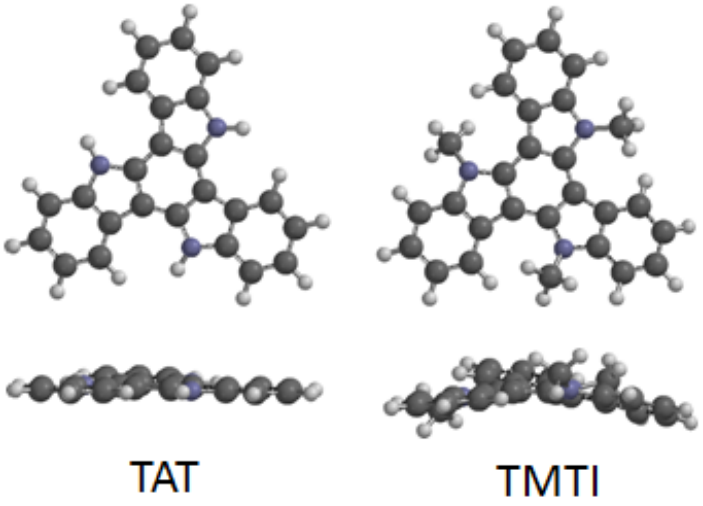

Figure 36 The molecular structures of TAT and TMTI given by DFT calculations, TAT shows much flatter molecular geometry than TMTI.[72]

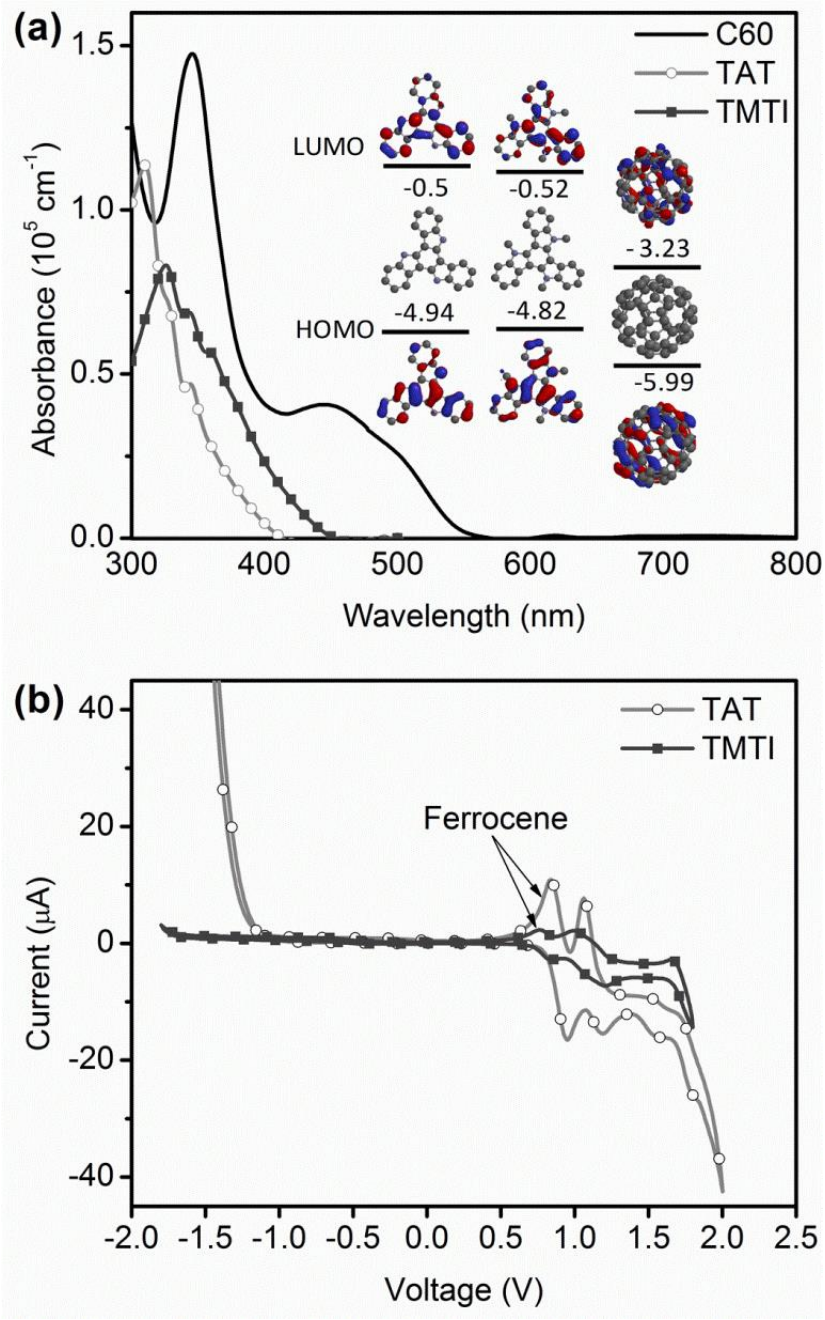

Figure 37 a) Absorption spectra of solution processed thin films of TAT and TMTI, and vapor deposited C60 film, the insert illustrates orbital energy levels in vacuum, minimum energy conformations, and electron density plots by DFT calculations; b) cyclic voltammetry curves of TAT and TMTI in dichloromethane solution with ferrocene as internal reference.[72]

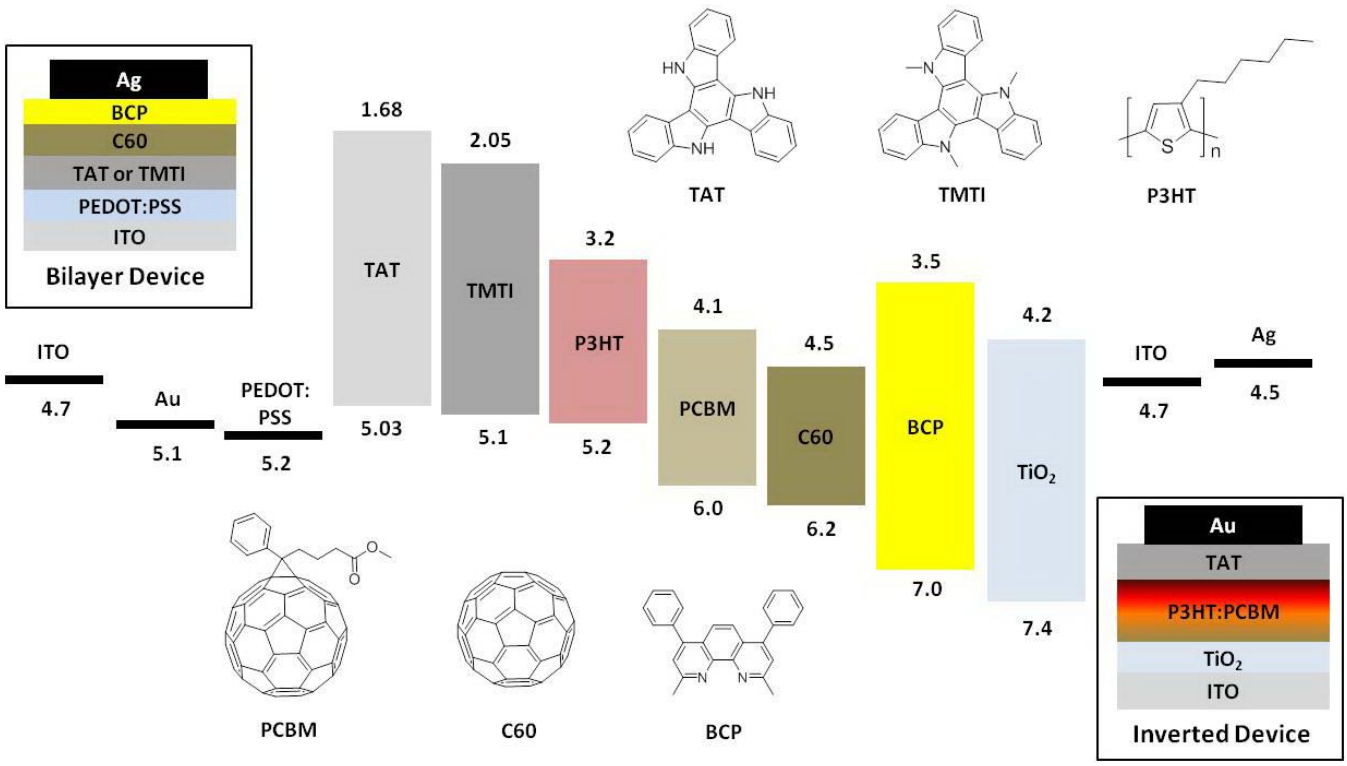

Figure 38 Chemical structures and energy levels of all materials used in this study; schematic device structures of bilayer and inverted devices.[72]

Thin film topology was characterized using atomic force microscopy (AFM). Figure 39 shows the AFM images for the solution processed thin films both before and after thermal annealing at 120 °C for 10 minutes. It was found that both molecules could form relatively smooth and continuous filmsvia solution processing, with root-mean-square (rms) roughness of ~ 1.3 nm for TAT and ~ 0.4 nm for TMTI respectively. The TAT film showed more crystalline features than TMTI, which is not surprising considering the hydrogen bonding effect. Thermal annealing was found to have negligible impact on the surface roughness, which prevented the device breakdown by film cracking. Hole carrier mobility of these films was evaluated by space-charge-limited-current measurements, yielding hole mobility of ~ 10^{-5}-10^{-4} $cm^2V^{-1}s^{-1}$, enough for efficient hole transport in organic solar cells. Thermal annealing slightly improved the hole mobility.

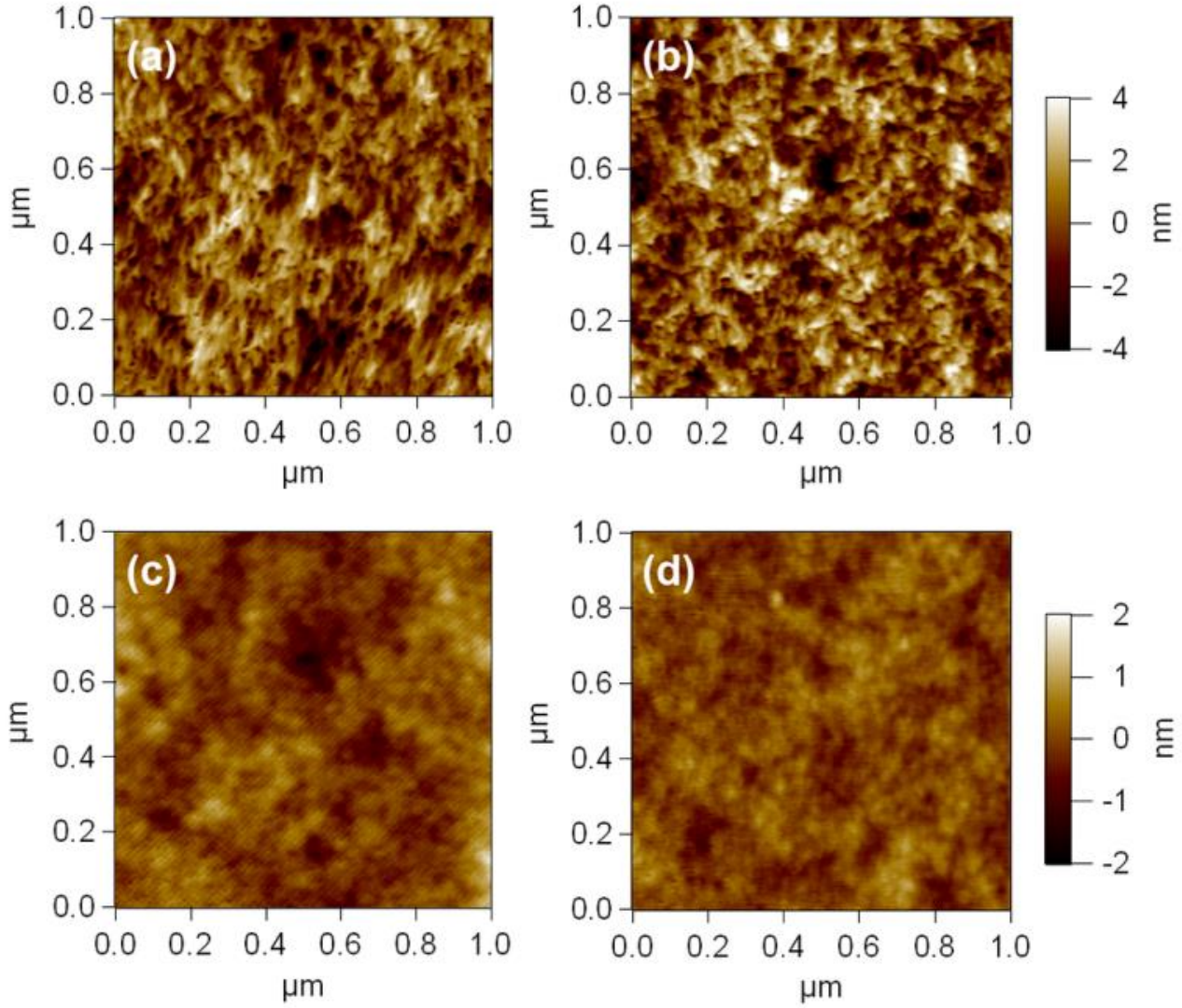

Figure 39 Tapping mode AFM topographical images of solution processed TAT (a, b) and TMTI (c, d). While (a) and (c) represent thin films before thermal annealing, (b) and (d)represent films after thermal annealing at 120 °C for 10 minutes.[72]

4.5 Hole Mobility Measurements

The hole mobility was measured by fabricating hole-only devices with an architecture of ITO/PEDOT:PSS/triindole/Au. These devices were fitted with the field-dependent space charge limited current (SCLC) method, which is described by

$$J_{SCLC} = \frac{9}{8}\varepsilon_r\varepsilon_0\mu_{h0}e^{0.89\gamma\sqrt{E}}\frac{V^2}{L^3} \quad (1.12)$$

wherein ε_0 is the permittivity of space, ε_R is the dielectric constant of the molecule (assumed to be 3), μ_{h0} is the zero-field hole mobility, γ is the field dependence prefactor, E is the electric field, V is the voltage drop across the device ($V=V_{applied}-V_{bi}-V_r$), and L is the active layer thickness. The series and contact resistance of the device was 20 Ω; so the voltage drop due to

this resistance (V_r) was subtracted from the applied voltage. The built-in voltage (V_{bi}) resulting from the difference in work function of the PEDOT:PSS and Au was assumed to be zero. Figure 40 shows the J-V curves representing the TMTI hole only device with TMTI thickness of ~ 88 nm. The SCLC hole mobility was calculated to be ~ 6-8 × 10^{-3} cm^2V^{-1} s^{-1} for TMTI with similar results for both the as cast and annealed films.

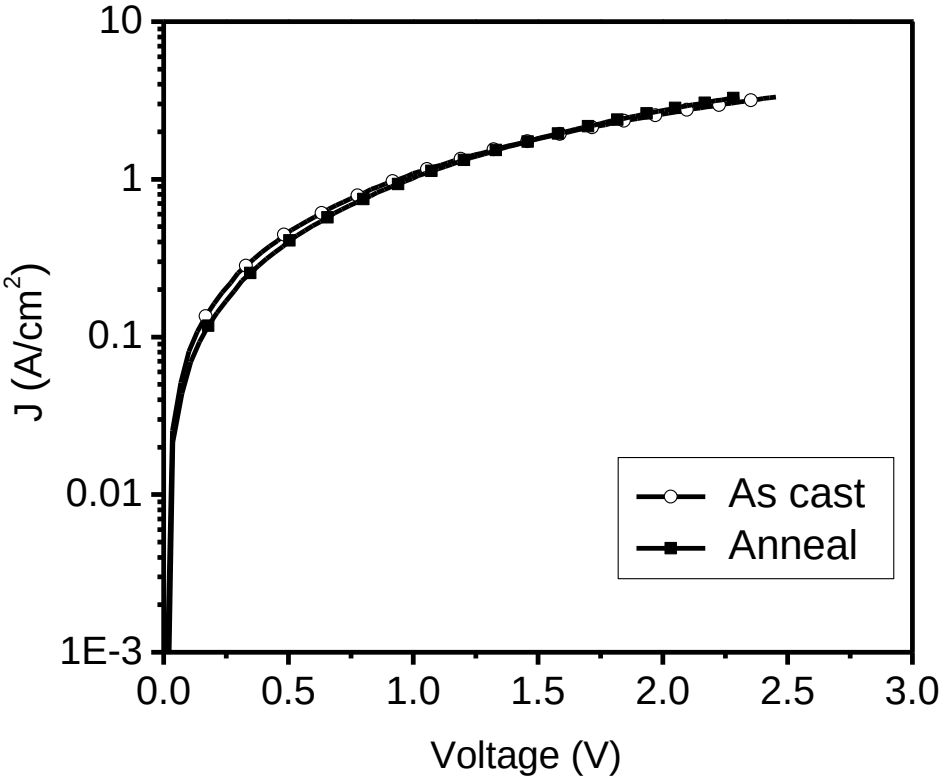

Figure 40 Current density-voltage *(J-V)* plots for ITO/PEDOT:PSS/TMTI/Au with thickness of 88 nm.[72]

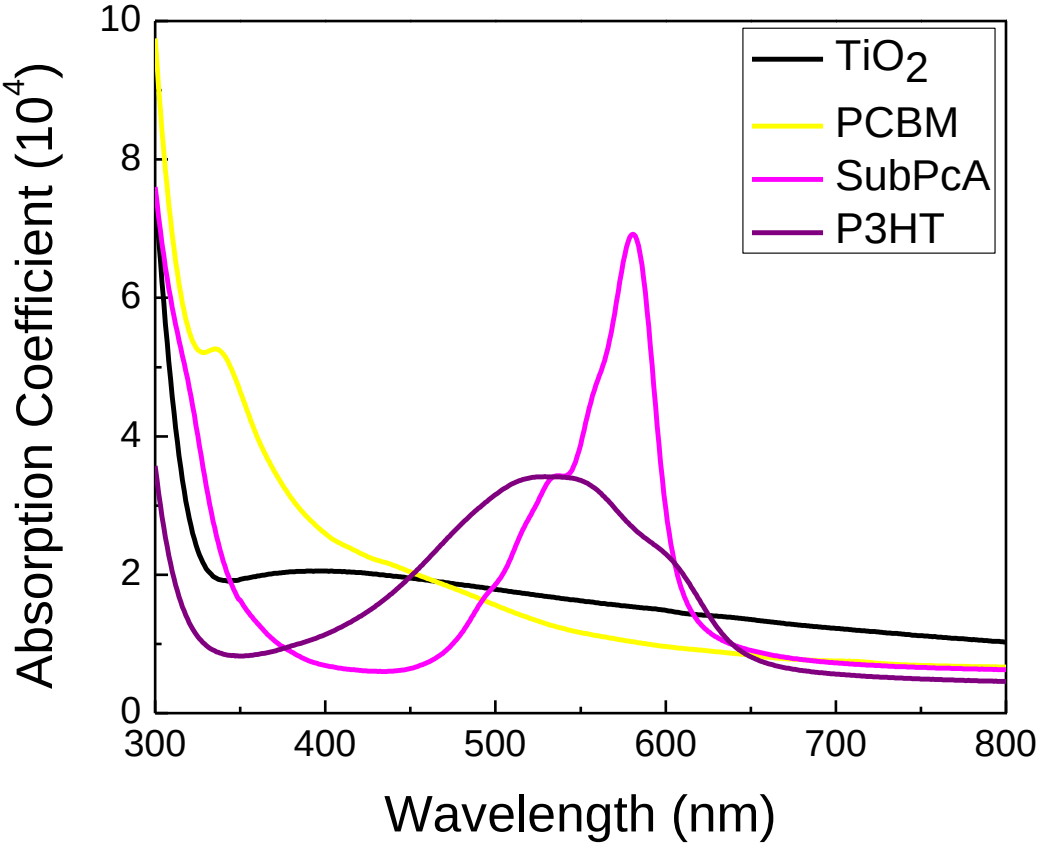

Figure 41 Absorption coefficient of several important materials: TiO_2, SubPc-A, PCBM, and P3HT.[72]

4.6 Bilayer Solar Cell Performance

We have tested the hole extracting/electron blocking capability of TAT and TMTI in devices with a simple planar heterojunction structure, ITO/PEDOT:PSS/TAT (or TMTI)/C60 (32 nm)/BCP (8 nm)/Ag (100 nm) as shown in Figure 38. A control device without the TAT (or TMTI) layer was fabricated as well. Due to its poor absorption in the visible region (Figure 37a), light harvesting and exciton generation in the TAT (or TMTI) layer is negligible. In other words, all the bilayer devices tested here are expected to have a preponderance of excitons generated in the C60 layer which undergo charge separation at the interfaces via hole transfer, instead of electron transfer occurring in typical planar heterojunction devices with excitons generated in the electron donor layer as shown in Figure 42.

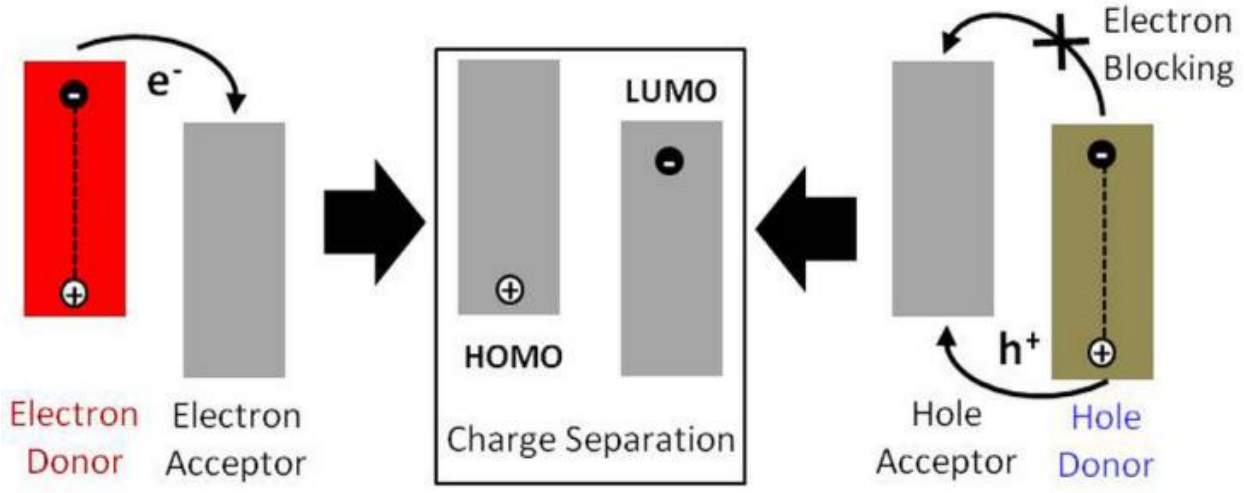

Figure 42 A schematic illustrating the two types of charge separation in the bilayer donor/acceptor interfaces.[72]

Figure 43 shows the device characteristics for the as-cast devices under AM 1.5 G simulated solar illumination at an intensity of 100 mW cm^{-2}; values are also listed in Table 1. The virtually identical shape of the EQE spectra for three devices supports the hypothesis that excitons are generated in the C60 layer. It is found that all figures of merit were enhanced significantly with the addition of a TAT (or TMTI) layer. For instance, power conversion efficiency (PCE) improved from 0.12 % to 0.65 %; and the external quantum efficiency (EQE) at 450 nm improved from about 12 % to over 25 %. These dramatic improvements were primarily attributable to the superior hole extracting and electron/exciton blocking capabilities of the TAT (or TMTI) layer. First, the large energy gap between the HOMO levels of TAT (or TMTI) at ~ 5.1 eV and C60 at ~ 6.2 eV allowed for highly efficient hole extraction. Secondly, the extremely high LUMO levels (-1.68 eV for TAT and -2.05 eV for TMTI) could easily block electrons from C60 which has a much lower LUMO level of - 4.5 eV. This blocking effect is also evidenced by the diminished dark current upon the addition of this TAT (or TMTI) layer as shown in Figure 43b. Thirdly, the hole mobility of the TAT (or TMTI) layer is comparable with the electron mobility of the C60 layer, which ensured balanced hole/electron concentration with reduced charge recombination. Lastly, the high bandgap of TAT (or TMTI) also led to exciton blocking capability that prevents exciton leakage to the anode.

Further efficiency enhancement has been achieved by thermal annealing. The device characteristics of all these devices before and after thermal annealingat 120˚C for 10 minutes are summarized in Table 1. The enhanced molecular organization in the TAT (or TMTI) upon thermal annealing is likely responsible for the improved hole transport and hole/electron balance. Although the overall efficiency is still much lower than that of state-of-the-art bilayer devices, a new type of "hole only" device is well presented here, wherein the solar light is mainly harvested by the electron acceptor (or hole donor) layer and excitons are efficiently dissociated at the interfaces via hole transfer through HOMO levels. I believe that an electron acceptor, with similar electronic properties as C60 but better light harvesting, would deliver higher performance based on this "hole only" type of device.

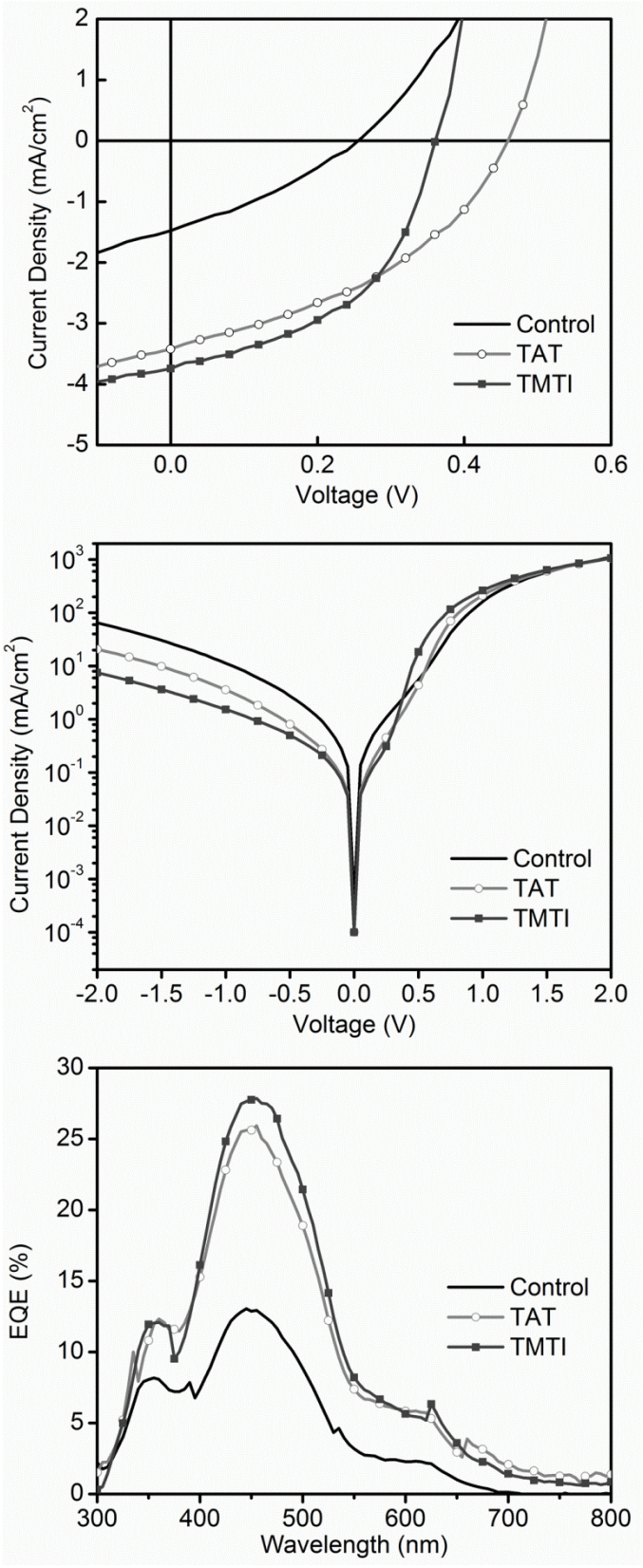

Figure 43 a) Current density-voltage (*J-V*) performance of bilayer devices with and without TAT or TMTI layer under light, b) *J-V* curves of those devices under dark, c) EQE spectra for those devices.[72]

Table 1 Device characteristics of organic solar cells under 1 sun AM 1.5 simulated illumination.[72]

Device	Bilayer devices (ITO/PEDOT:PSS/X/C60/BCP/Ag)			Inverted devices (ITO/TiO2/P3TH:PCBM/X/Au)	
Interlayer	N/A	TAT	TMTI	N/A	TAT
V_{oc} (V)	0.26 (0.26)	0.41 (0.47)	0.36 (0.48)	0.41	0.43
J_{sc} (mA/cm2)	1.45(1.67)	3.28 (3.57)	3.74 (3.89)	6.44	8.04
FF	0.31(0.37)	0.48(0.43)	0.48(0.47)	0.40	0.39
PCE (%)	0.12(0.16)	0.65(0.71)	0.65(0.87)	1.06	1.34

4.7 Inverted Solar Cells

The application of TAT as an interfacial layer in inverted solar cells, wherein a common P3HT:PCBM blend acts as the photoactive layer, was also investigated. The substantial solubility of TAT in methanol allowed for sequential deposition of multilayers using orthogonal solvents. Specifically, an inverted solar cell with the architecture of ITO/TiO_2(70 nm)/P3HT:PCBM (100 nm)/TAT(<5 nm)/Au (50 nm) was fabricated, wherein the P3HT:PCBM layer was spin cast in chlorobenzene solution and TAT in methanol solution. The thickness of the TAT layer was dictated by the solution concentration. The best performing device was fabricated by spin-coating a solution of TAT in methanol (2 mg/ml) at 2000 rpm for 40 seconds. A control device absent of TAT was built for comparison and the results are displayed in Table 1. It is easily observed that the addition of the TAT interfacial layer increases the short circuit current from 6.44 to 8.04 mA cm^{-2} by selecting for holes and rejecting electrons at the Au electrode. This behavior is commensurate with a slight rise in V_{oc}, as a result of the decreased recombination. There was not a significant change to the fill factor because such a thin layer of TAT did not substantially affect the series resistance of the P3HT/Au junction. Overall, the power conversion efficiency increases by 26%, from 1.06% to 1.34%. This behavior is again illustrated in the EQE spectrum where the rise is shown mainly from 500 nm-600 nm, the same region in which P3HT:PCBM absorption dominates. Overall, the additional current results not from the light harvesting of TAT but from improved charge selection in the anode.

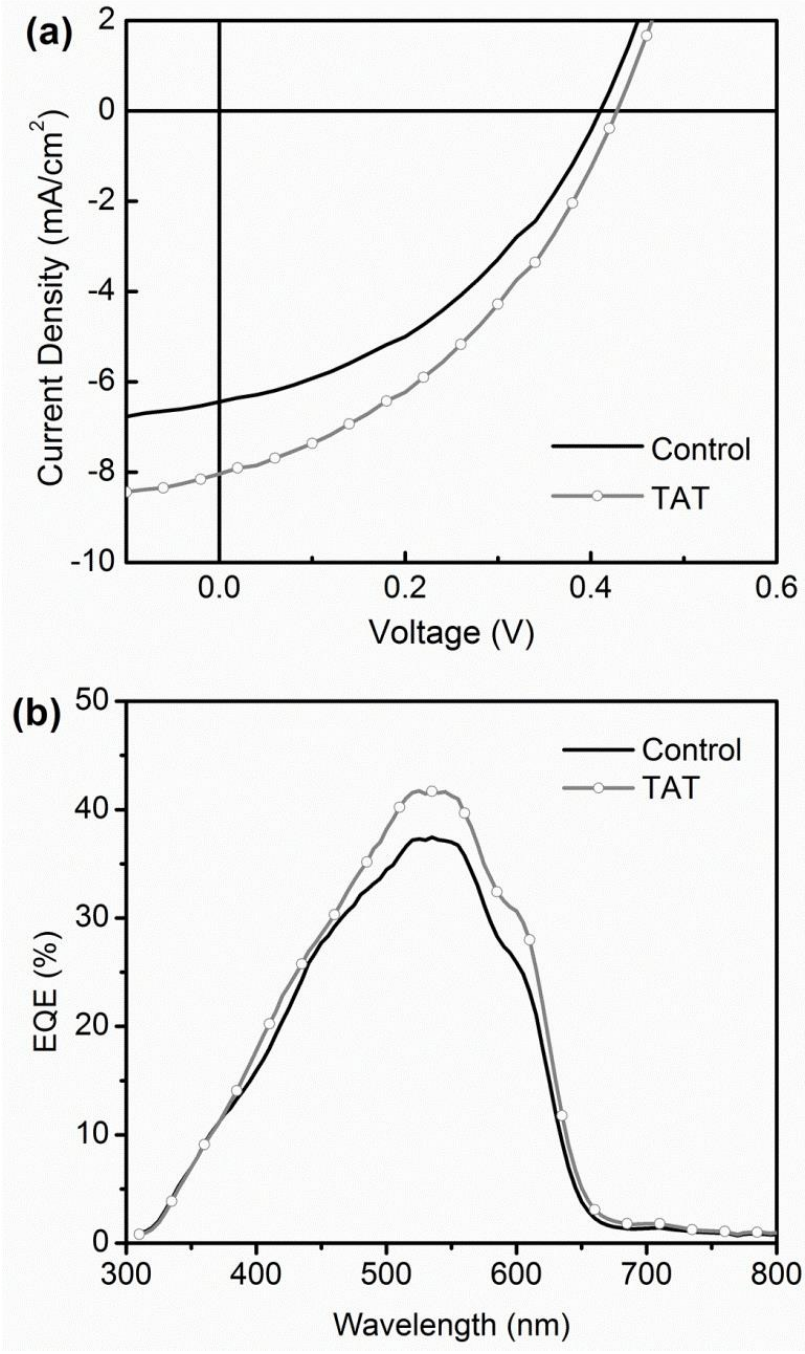

Figure 44 a) Current density-voltage (*J-V*) behavior of inverted devices with and without TAT layer under light, b) *J-V* curves of the devices under dark.[72]

Chapter 5
Conclusion

5.1 Summary of Results

The work of this dissertation has dealt with interfacial engineering at the donor-acceptor interface and at the donor-anode interface. In Chapter 1, nanostructuring of SubPc-A was proven feasible via nanoimprint lithography. Successful incorporation of this material into a solar cell requires not just considerations of the nanoscale morphology but also the energetics. The energy levels of SubPc-A must form a type II band alignment with the acceptor material in order for electrons to cascade down towards the cathode and holes to cascade up towards the anode. Such a nanostructured donor material is certainly compatible with acceptor materials deposited by evaporation that can preserve the integrity of the nanostructured film.

Chapter 2 considered extending the nanostructuring concept to two-component donors with the intention of broadening the absorption spectrum of the solar cell. Based on energetics as well as compatibility with the technique of nanoimprint lithography, the suitable material combinations were BOADPM/SQ and BOADPM/SubPc-A. BOADPM was proven capable of serving as a host matrix as it can be nanoimprinted like SubPc-A. With the above material combinations, the near-infrared absorption of BOADPM could be extended into the visible with the incorporation of SQ or SubPc-A.

In Chapter 3, solution processable, transparent, organic hole-selective materials, triazatruxene (TAT) and N-trimethyltriindole (TMTI)were synthesized, characterized and tested. Their excellent hole extracting and conducting, as well as electron and exciton blocking capabilities were clearly demonstrated for the first time in organic solar cells with significantly enhanced device performance. For example, the insertion of a hole selective layer between PEDOT:PSS and C60 layers in “hole only” planar heterojunction devices has increased the power conversion efficiency from 0.16% to 0.71% for TAT and 0.87% for TMTI, respectively. Methanol-soluble TAT was also used in an inverted P3HT:PCBM/TiO_2 device, wherein the efficiency improved from 1.06% to 1.34% simply by adding the interlayer. The present results show that triindole-based molecules are highly promising hole selective materials with a high LUMO level, modest HOMO level and high hole mobility, which could easily be incorporated to other organic electronic devices. Continuing efforts deal with the development of various derivatives, such as crosslinkable ones that could be solution processed and converted into insoluble thin films for multilayer structures; and functionalized ones that could form self-assembled monolayers on electrodes via covalent binding.

5.2 Outlook for Further Study

If nanoimprinting is an effective way to improve solar cell performance, more charges will be collected for every absorbed photon. Once the exciton is generated in the donor, presumably it is more likely to diffuse towards and actually reach an interface compared to its

bulk counterpart. For that reason, more excitons will be split and more total charges will be collected at the electrodes. Therefore, the most effective measurement to test for this behavior is an internal quantum efficiency measurement (Fig. 45a).

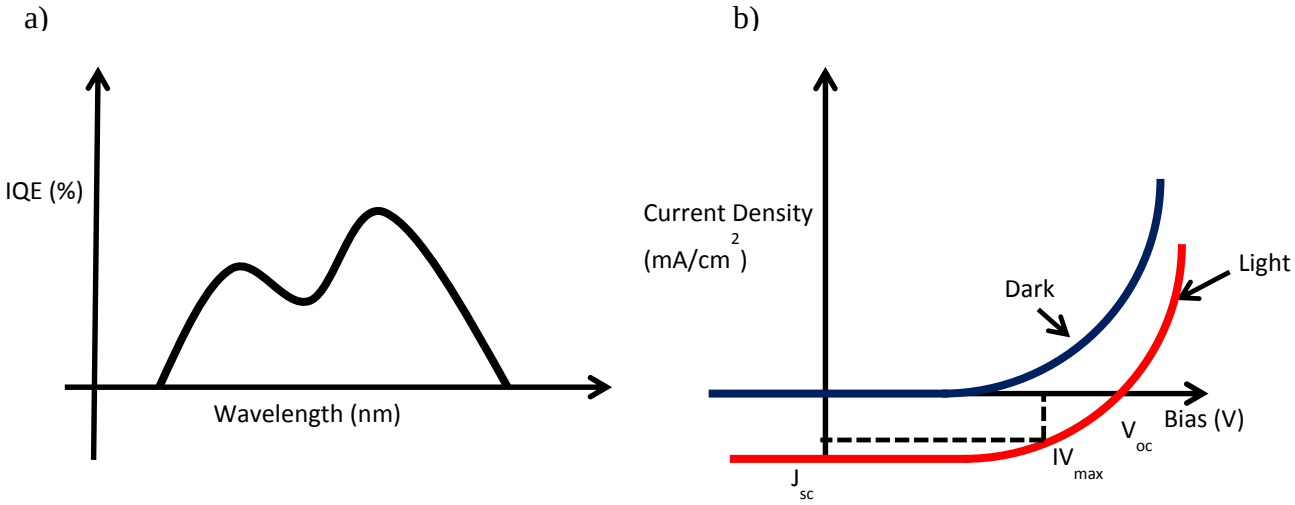

Fig. 45 a) Schematic of an internal quantum efficiency measurement (IQE) b) Schematic of an IV measurement, including a measurement in the dark and one under 1 sun illumination

The improvement may also be evident in the overall IV performance, but there is no guarantee. Such behavior would also require that the amount of absorbed light is exactly the same between the two devices being compared; there is no certainty of that as the thickness can vary between samples to a significant degree.

Nanoimprinting may result in unintended consequences that affect the overall device performance. After all, the pressure and temperature are both elevated. It is entirely reasonable that, most notably, the crystallinity of the film can change. This is of consequence because the crystallinity changes the mobility.[57-68] If the mobility rises, for example, the boost in performance may be attributable, at least in part, to this intrinsic property rather than the nanostructured architecture. It is necessary to decouple these effects by measuring the mobility and gauging the degree of crystallinity with x-ray diffraction before and after subjecting the film to the elevated temperature and pressure (200°C, and 200 Pa). The x-ray diffraction pattern will readily show any pressure-induced crystallinity, as SubPc-A, BOADPM, and SQ are all amorphous in their as-cast state. For that reason, the simple observation of peaks in the diffraction pattern after processing will provide binary evidence of such pressure-induced crystallinity since the as-cast films have no peaks. The properties of a pristine film will be compared to a film subjected to the heat and pressure during the nanoimprinting process to see if there is a difference due to processing.

Bibligraphy

1. Tang, C. W. *Appl. Phys. Lett.* **1986,** *48* (2), 183-185.

2. G. Yu, J. Gao, J.C. Hummelen, F. Wudl, A.J. Heeger. *Science*. **1995**, 270, 1789.

3. R. Kersting, U. Lemmer, M. Deussen, H. J. Bakker, R. F. Mahrt, H. Kurz, V. I. Arkipov, H. Bässler, E. O. Göbel. *Phys Rev Lett.* **1994**, 73, 10, 1440.

4. A.C. Mayer, S. R. Scully, B. E. Hardin, M. W. Rowell, and M.D. McGehee. *Materials Today*. **2007**, 10, 11.

5. C. Goh, R. J. Kline, M.D. McGehee, E. N. Kadnikova, and J. M. J. Fréchet. *Appl. Phys. Lett.* **2005**, *86*, 122110.

6. D. Muhlbacher, M. Scharber, M. Morana, Z. Zhu, D. Waller, R. Gaudiana, C. Brabec. *Adv. Mater.* **2006,** 18 **,** 2884–2889.

7. S. Y. Leblebici, L. Catane, D. E. Barclay, T. Olson, T. L. Chen, B. W. Ma. *ACS Appl. Mater. Interfaces.* **2011**, 3, 4469.

8. G. Li, R. Zhu, Y. Yang. *Nature Photonics*. **2012**, 6.

9. A.C. Mayer, M. F. Toney, S. R. Scully, J. Rivnay, C. J. Brabec, M. Scharber, M. Koppe, M. Heeney, I. McCulloch, M. D. McGehee. *Adv. Funct. Mater.* **2009**, 19, 1173-1179.

10. G. Li, V. Shrotriya, J. Huang, Y. Yao, T. Moriarty, K. Emery, Y. Yang. *Nature Materials*. **2005**, 4.

11. F. Yang, M. Shtein, S. R. Forrest. *Nature*. **2005**, 4, 37.

12. M. T. Lloyd, J. E. Anthony, G. G. Malliaras. *Materials Today*. **2007**, 10, 11, 34-41.

13. M. Hirade, H. Nakanotani, M. Yahiro, C. Adachi. *ACS Appl. Mater. Interfaces*. **2011**, 3, 1, 80.

14. J. Weickert, R. B. Dunbar, H. C. Hesse, W. Wiedemann, L. Schmidt-Mende. *Adv. Mater.* **2011**, 23, 1810.

15. F. S. Bates. *Annu. Rev. Phys. Chem.***1990**, 41, 525-57.

16. X. Gu, Z. Liu, I. Gunkel, S.T. Chourou, S. W. Hong, D. L. Olynick, T. P. Russell. *Adv. Mat.* **2012**, 24, 568-5694.

17. B. Ma, Y. Miyamoto, C. H.Woob, J. M. J. Frèchet, F. Zhang, Y. Liu. *Proc. SPIE.* **2009**, *7416*, 74161E.

18. X. Liang, T. Chen, Y. Jung, Y. Miyamoto, G. Han, S. Cabrini, B. W. Ma, D. L. Olynick. *ACS Nano*. **2010**, 4, 5, 2627.

19. L. Hu, Z. Yan, H. Xu. *RSC Advances*. **2013**, 3, 7667.

20. G. Wei, R. R. Lunt, K. Sun, S. Wang, M. E. Thompson, S. R. Forrest. *Nanoletters*. **2010**, 10, 3555-3559.

21. A. Haugeneder, M. Neges, C. Kallinger, W. Spirkl, U. Lemmer, J. Feldmann. *Phys. Rev. B.* **1999**, 59, 23.

22. P. Peumans, A. Yakimov, S. R. Forrest. *Journal of Appl. Phys.* **2003**, 93, 3693

23. K. J. Bergemann, S. R. Forrest. *Appl. Phys. Lett.* **2011**, 99, 243303.

24. D. Olynick, J. A. Liddle, B. D. Harteneck, S. Cabrini, I. W. Rangelow. *Proc. Of SPIE.* **2007**, 6462.

25. B. P. Rand, J. Li, J. G. Xue, R. J. Holmes, M. E. Thompson, S. R. Forrest. *Adv Mater.* **2005,** *17*, 22, 2714.

26. M. Y. Chan, C. S. Lee, S. L. Lai, M. K. Fung, F. L. Wong, H. Y. Sun, K. M. Lau, S.T. Lee. *J Appl Phys.* **2006,** *100*, 9.

27. S. Khodabakhsh, B. M. Sanderson, J. Nelson, T. S. Jones. *Adv Funct Mater.* **2006,** *16*, 1, 95-100.

28. M. D. Irwin, B. Buchholz, A. W. Hains, R. P. H. Chang, T. J. Marks. *P Natl Acad Sci USA.* **2008,** *105*, 8, 2783-2787.

29. J. Subbiah, D. Y. Kim, M. Hartel, F. So. *Appl Phys Lett.* **2010,** *96*, 6.

30. G. Li, C. W. Chu, V. Shrotriya, J. Huang, Y. Yang.*Appl Phys Lett.* **2006,** *88*, 25.

31. C. T. Tseng, Y. H. Cheng, M. C. M. Lee, *Appl Phys Lett.* **2007,** *91*, 23.

32. J. S. Huang, C. Y. Chou, M. Y. Liu, K. H. Tsai, W. H. Lin, C. F. Lin. *Org Electron.* **2009,** *10*, 6, 1060-1065.

33. C. Tao, S. P. Ruan, G. H. Xie, X. Z. Kong, L. Shen, F. X. Meng, C. X. Liu, X. D. Zhang,W. Dong, W. Y. Chen. *Appl Phys Lett.* **2009,***94*, 4.

34. Y. Gao, H. L. Yip, S. K. Hau, K. M. O'Malley, N. C. Cho, H. Z. Chen, A. K. Y. Jen. *Appl Phys Lett.* **2010,** *97*, 20.

35. E. D. Gomez,Y. L. Loo. *J Mater Chem.* **2010,** *20*, 32, 6604-6611.

36. A. W. Hains, J. Liu, A. B. F. Martinson, M. D. Irwin, T. J. Marks. *Adv Funct Mater.* **2010,** *20*, 4, 595-606.

37. S. O. Jeon, K. S. Yook, B. D. Chin, Y. S. Park, J. Y. Lee. *Sol Energ Mat Sol C.* **2010,** *94*, 8, 1389-1392.

38. S. S. Li, K. H. Tu, C. C. Lin, C. W. Chen, M. Chhowalla. *Acs Nano.* **2010,** *4*, 6, 3169-3174.

39. R. Steim, F. R. Kogler, C. J. Brabec. *J Mater Chem.* **2010,** *20*, 13, 2499-2512.

40. E. L. Ratcliff, B. Zacher, N. R. Armstrong. *J Phys Chem Lett.* **2011,** *2*, 11, 1337-1350.

41. Y. M. Sun, X. O. Gong, B. B. Hsu, H. L. Yip, A. K. Y. Jen, A. J. Heeger. *Appl Phys Lett* **2010,** *97*, 19.

42. Y. M. Sun, M. F. Wang, X. O. Gong, J. H. Seo, B. B. Y. Hsu, F. Wudl, A. J. Heeger, *J Mater Chem.* **2011,** *21*, 5, 1365-1367.

43. K. X. Steirer, J. P. Chesin, N. E. Widjonarko, J. J. Berry, A. Miedaner, D. S. Ginley, D. C. Olson. *Org Electron.* **2010,** *11*, 8, 1414-1418.

44. R. Betancur, M. Maymo, X. Elias, L. T. Vuong, J. Martorell. *Sol Energ Mat Sol C.* **2011,** *95*, 2, 735-739.

45. M. Hirade, C. Adachi, *Appl Phys Lett.* **2011,** *99*, 15.

46. M. D. Irwin, J. D. Servaites, D. B. Buchholz, B. J. Leever, J. Liu, J. D. Emery, M. Zhang, J. H. Song, M. F. Durstock, A. J. Freeman, M. J. Bedzyk, M. C. Hersam, R. P. H. Chang, M. A. Ratner, T. J. Marks, *Chem Mater.* **2011,** *23*, 8, 2218-2226.

47. B. E. Lassiter, G. D. Wei, S. Y. Wang, J. D. Zimmerman, V. V. Diev, M. E. Thompson, S. R. Forrest. *Appl Phys Lett.* **2011,** *98*, 24.

48. I. P. Murray, S. J. Lou, L. J. Cote, S. Loser, C. J. Kadleck, T. Xu, J. M. Szarko, B. S. Rolczynski, J. E. Johns, J. X. Huang, L. P. Yu, L. X. Chen, T. J. Marks, M. C. Hersam. *J Phys Chem Lett.* **2011,** *2*, 24, 3006-3012.

49. M. Reinhard, J. Hanisch, Z. H. Zhang, E. Ahlswede, A. Colsmann, U. Lemmer. *Appl Phys Lett.* **2011,** *98*, 5.

50. J. H. Seo, A. Gutacker, Y. M. Sun, H. B. Wu, F. Huang, Y. Cao, U. Scherf, A. J. Heeger, G. C. Bazan. *J Am Chem Soc.* **2011,** *133*, 22, 8416-8419.

51. K. X. Steirer, P. F. Ndione, N. E. Widjonarko, M. T. Lloyd, J. Meyer, E. L. Ratcliff, A. Kahn, N. R. Armstrong, C. J. Curtis, D. S. Ginley, J. J. Berry, D. C. Olson. *Adv Energy Mater.* **2011,** *1*, 5, 813-820.

52. K. Zilberberg, S. Trost, J. Meyer, A. Kahn, A. Behrendt, D. Lutzenkirchen-Hecht, R. Frahm, T. Riedl. *Adv Funct Mater.* **2011,** *21*, 24, 4776-4783.

53. K. Zilberberg, S. Trost, H. Schmidt, T. Riedl. *Adv Energy Mater.* **2011,** *1*, 3, 377-381.

54. H. Kageyama, H. Ohishi, M. Tanaka, Y. Ohmori, Y. Shirota. *Appl Phys Lett.* **2009,** *94*, 6.

55. G. Zhang, W. L. Li, B. Chu, L. L. Chen, F. Yan, J. Z. Zhu, Y. R. Chen, C. S. Lee. *Appl Phys Lett.* **2009,** *94*, 14.

56. S. Berny, L. Tortech, M. Veber, D. Fichou. *Acs Appl Mater Inter.* **2010,** *2*, 11, 3059-3068.

57. L. S. C. Pingree, B. A. MacLeod, D. S. Ginger. *J Phys Chem C.* **2008,** *112*, 21, 7922-7927.

58. Feng, G. L.; Lai, W. Y.; Ji, S. J.; Huang, W., Synthesis of novel star-shaped carbazole-functionalized triazatruxenes. *Tetrahedron Lett.* **2006,** *47* (39), 7089-7092.

59. W. Y. Lai, R. Zhu, R. Q. L. Fan, L. T. Hou, Y. Cao, W. Huang. *Macromolecules.* **2006,** *39*, 11, 3707-3709.

60. B. Gomez-Lor, B. Alonso, A. Omenat, J. L. Serrano. *Chem Commun.* **2006,** 48, 5012-5014.

61. B. Gomez-Lor, G. Hennrich, B. Alonso, A. Monge, E. Gutierrez-Puebla, A. M. Echavarren. *Angew Chem Int Edit.* **2006,** *45*, 27, 4491-4494.

62. E. M. Garcia-Frutos, B. Gomez-Lor. *J Am Chem Soc.* **2008,** *130*, 28, 9173-9177.

63. M. Talarico, R. Termine, E. M. Garcia-Frutos, A. Omenat, J. L. Serrano, B. Gomez-Lor, A. Golemme. *Chem Mater.* **2008,** *20*, 21, 6589-6591.

64. W. Y. Lai, Q. Y. He, D. Y. Chen, W. Huang. *Chem Lett.* **2008,** *37*, 9, 986-987.

65. E. M. Garcia-Frutos, E. Gutierrez-Puebla, M. A. Monge, R. Ramirez, P. de Andres, A. de Andres, R. Ramirez, B. Gomez-Lor. *Org Electron.* **2009,** *10*, 4, 643-652.

66. B. M. Zhao, B. Liu, R. Q. Png, K. Zhang, K. A. Lim, J. Luo, J. J. Shao, P. K. H. Ho, C. Y. Chi, J. S. Wu. *Chem Mater.* **2010,** *22*, 2, 435-449.

67. T. Bura, N. Leclerc, S. Fall, P. Leveque, T. Heiser, R. Ziessel. *Org Lett.* **2011,** *13*, 22, 6030-6033.

68. E. M. Garcia-Frutos, A. Omenat, J. Barbera, J. L. Serrano, B. Gomez-Lor. *J Mater Chem* **2011,** *21*, 19, 6831-6836.

69. F. Gallego-Gomez, E. M. Garcia-Frutos, J. M. Villalvilla, J. A. Quintana, E. Gutierrez-Puebla, A. Monge, M. A. Diaz-Garcia, B. Gomez-Lor. *Adv Funct Mater.* **2011,** *21*, 4, 738-745.

70. M. Franceschin, L. Ginnari-Satriani, A. Alvino, G. Ortaggi, A. Bianco. *Eur J Org Chem.* **2010,** 1, 134-141.

71. B. W. D'Andrade, S. Datta, S. R. Forrest, P. Djurovich, E. Polikarpov, M. E. Thompson. *Org Electron.* **2005,** *6*, 1, 11-20.

72. S. W. Shelton, T. L. Chen, D. E. Barclay, B. Ma. *ACS Appl Mater Interfaces.* **2012,** 4, 5, 2534-40.